AEDC-TDR-63-270

EXPERIMENTAL AND ANALYTICAL INVESTIGATION OF THE EFFECT OF CRYODEPOSITS ON THE RADIATION PROPERTIES OF PLAIN AND EXTENDED SURFACES

By

R. P. Caren, A. S. Gilcrest, C. A. Zierman
W. F. Schmidt, and J. P. Millard
Aerospace Sciences Laboratory
Lockheed Missiles & Space Co., Palo Alto, California

TECHNICAL DOCUMENTARY REPORT NO. AEDC-TDR-63-270

December 1963

Program Area 850E, Project 7778, Task 777801

(Prepared under Contract No. AF 40(600)-992 by Aerospace Sciences Laboratory, Lockheed Missiles & Space Co., Palo Alto, Calif.)

ARNOLD ENGINEERING DEVELOPMENT CENTER
AIR FORCE SYSTEMS COMMAND
UNITED STATES AIR FORCE

NOTICES

Qualified requesters may obtain copies of this report from DDC, Cameron Station, Alexandria, Va. Orders will be expedited if placed through the librarian or other staff member designated to request and receive documents from DDC.

When Government drawings, specifications or other data are used for any purpose other than in connection with a definitely related Government procurement operation, the United States Government thereby incurs no responsibility nor any obligation whatsoever; and the fact that the Government may have formulated, furnished, or in any way supplied the said drawings, specifications, or other data, is not to be regarded by implication or otherwise as in any manner licensing the holder or any other person or corporation, or conveying any rights or permission to manufacture, use, or sell any patented invention that may in any way be related thereto.

AEDC-TDR-63-270

EXPERIMENTAL AND ANALYTICAL INVESTIGATION OF THE EFFECT OF CRYODEPOSITS ON THE RADIATION PROPERTIES OF PLAIN AND EXTENDED SURFACES

By

R. P. Caren, A. S. Gilcrest, C. A. Zierman

W. F. Schmidt, and J. P. Millard

Aerospace Sciences Laboratory

Lockheed Missiles and Space Co., Palo Alto, California

December 1963

(The reproducibles used in the reproduction of this report were supplied by the authors.)

AF - AEDC
Arnold AFS Tenn

FOREWORD

This report was prepared by the Thermophysics section of the Aerospace Sciences Laboratory, The Research Organization, Lockheed Missiles & Space Company, for the Arnold Engineering Development Center, Air Force Systems Command, United States Air Force. The work was performed under contract AF 40(600)-992, Project No. 7778, Task 777801. The contract was administered by Space Systems Office, Arnold Engineering Development Center, Arnold Air Force Station, Tennessee.

This report describes work conducted from 15 June 1962 to 15 August 1963.

The program was carried out under the direction of R. E. Gaumer, with R. P. Caren as Project Scientist. The calorimeter, the vacuum system, the optical system, and the cryogen transfer systems were designed and constructed with the advice and assistance of J. P. Hardman and W. E. Morton. Development of the numerical methods and programming of the computer solutions for the integral equations for the effective emittance of the V-Groove were carried out by J. C. Fick, W. Chuck, E. Hansen, and B. Yoshikawa.

ABSTRACT

In the thermal design of a cryopumped space simulation chamber, the absorptance of the 77°K cold wall for solar and room temperature radiation and the absorptance of the 20°K cryowall for 77°K and reflected solar radiation should be considered. The absorptances of the above surfaces depend on the substrate material, type and thickness of the condensable gas deposited, the geometry of the surface, and the source of incident radiation.

Experiments for determining the cryo-deposited film heat transfer parameters and an analytic study of two extended surface configurations are described. The following investigations were made of: (1) hemispherical absorptance of water vapor and carbon dioxide deposits at 77°K for 290°K radiation as a function of deposit thickness, with plain aluminum and aluminum coated with a black epoxy paint as substrates, (2) normal absorptance of water vapor deposits at 77°K for radiation from a Mercury-Xenon source (with and without a filter) as a function of deposit thickness, with aluminum coated with a black epoxy as the substrate, and (3) hemispherical absorptance of nitrogen, dry air, and carbon dioxide deposits at 20°K with plain aluminum as the substrate. Analytic determinations of the effective absorptance (or emittance) of V-groove and honeycomb extended surface geometries were also made.

The results of the experimental data and of the analytical studies indicate that for a 80 to 100°K high absorptance cold wall, the ice and CO_2 deposits formed on this cold-wall surface will not appreciably reduce the absorptance of this surface and that the air, N_2, and CO_2 films condensed on a 20°K cryopumping surface will not significantly increase the thermal load on this surface.

This report has been technically reviewed and is approved for publication.

H. A. PERSON
Project Engineer
Space Systems Office

JOHN D. PETERS, Lt Col, USAF
Chief, Space Systems Office

CONTENTS

ILLUSTRATIONS

NOMENCLATURE

The following symbols are arranged in the order of their appearance in the text.

ϵ	total hemispherical emittance (dimensionless)
ϵ_{eff}	effective emittance of an extended surface (dimensionless)
$B(\_)$	radiosity of surface (_); emitted plus reflected energy flux leaving position (_)
σ	Stefan-Boltzmann constant
ρ	local reflectance of a surface
T	absolute temperature
$H(\_)$	flux incident on surface (_) due to energy leaving other surface of interest
θ	apex angle of V-groove
x, y, z	V-groove coordinates
L	V-groove leg length
$\beta(X)$	$B(x)/\epsilon\sigma T^4$, dimensionless radiosity
X	x/L, normalized length
Y	y/L, normalized length
Z	z/L, dimensionless width of a V-groove opening
$\bar{H}(Z)$	$H(z)/\epsilon\sigma T^4$, dimensionless energy incident on the V-groove opening equivalent to the energy leaving the V-groove
$\bar{M}$	M/L, dimensionless length where M is the width of the V-groove opening
τ	V-groove sighting angle
r_1	mean radiation per unit solid angle per unit projected area of a surface in the direction τ
R_1	dimensionless r_1
A	area
F	radiant energy configuration factor between two areas, F_{1-2} is the fraction of the total radiant flux leaving A_1 that is incident upon A_2
q	net heat transfer rate
$\bar{\epsilon}$	effective emittance of a composite surface consisting of both plain and extended sections
α	total hemispherical absorptance
$\dot{v}$	volumetric flow rate of calorimeter boil-off gas

d	density of either the calorimeter vapor or liquid
P	absolute pressure
W	edge length of honeycomb cell
t	thickness of honeycomb-cell material
M'	length of honeycomb cell
$P_{w.v.}$	vapor pressure of water
R	gas constant
H_v	heat of vaporization of calorimeter fluid
r_2	radius of calorimeter receiver head
t'	thickness of the cryodeposit on the calorimeter receiver head
m	weight of the cryodeposit
V	total volume of the cryodeposit gas storage reservoir

Section 1
INTRODUCTION

To provide adequate simulation of the space environment in a large space chamber, the absorptance of the chamber cold wall for both solar and room-temperature radiation must be close to unity. The refrigeration load on cryopumping surfaces should be known; this load includes radiation from the cold wall and simulated solar radiation reflected via the cold-wall surfaces. The absorptance of the cold-wall surface depends on the nature of the substrate coating, the surface geometry, the type and thickness of the condensable gas deposited, and the source of the incident radiation. The thermal energy absorbed at the cryopumping surface depends on the nature of the surface, the chamber geometry, the reflection coefficient of the cold wall for solar radiation, the emittance of the cold wall at its operating temperature, and the nature and thickness of the deposit on the cryopumping surface.

It is assumed that the cold wall of the space chamber operates in the temperature range from 80 to 100°K so that the primary deposit on this surface will be H_2O and some CO_2. To achieve chamber pressures below 10^{-9} Torr, the cryopumping surface must operate at 20°K or below. It is further assumed that the primary gas deposits on this surface will be N_2, O_2, and CO_2.

In order that the thermal radiative properties of cold and cryopumping walls can be predicted for the design of space simulation chambers, the following investigations were made in the present work: (1) The hemispherical absorptance of water vapor and carbon dioxide deposits at 77°K for 290°K radiation was measured as a function of deposit thickness. (2) The normal absorptance of water vapor deposits at 77°K for radiation from a Mercury-Xenon source (simulated solar radiation) was measured as a function of deposit thickness. (3) The hemispherical absorptance of air, CO_2, and nitrogen deposits at 20°K for 77°K blackbody radiation was measured. (4) The effect of geometry on the effective absorptance of two extended surface configurations was investigated.

Section 2
ABSORPTANCE OF 77°K H_2O and CO_2 FILMS FOR 290°K BLACKBODY AND SIMULATED SOLAR RADIATION

2.1 EXPERIMENTAL APPARATUS

The total hemispherical radiation calorimeter used for measuring the absorptance of 77°K H_2O and CO_2 condensates for 290°K blackbody and simulated solar radiation is shown in Figs. 1 through 3. The calorimetric portion of the apparatus consists of an outer guard reservoir, an inner guard reservoir, a receiver assembly, and a radiator assembly. The receiver assembly consists of a 300 ml-capacity copper cryogen reservoir to which various receiver heads can be bolted. The single thin wall stainless steel re-entrant tube supporting the receiver assembly is used both as a cryogen fill and boil-off line. The thermal energy incident on the receiver is measured by the boil-off rates of the contained liquid cryogen. The receiver assembly is thermally isolated from its surroundings by enclosing the entire calorimeter assembly in a vacuum chamber and surrounding the receiver by an inner guard reservoir operated at the receiver temperature. Temperature equality is assured by filling the inner guard reservoir with the same cryogenic fluid as the receiver reservoir. Additionally, the inner guard reservoir is thermally grounded to a section of the receiver assembly support tube by means of a heat exchanger made of compressed brass wool. This thermal short intercepts heat conducted down the support tube which would otherwise be conducted to the receiver reservoir.

The radiator consists of a 300 ml-capacity copper reservoir through which water is circulated for the 290°K blackbody work. The blackbody radiator head, consisting of a honeycomb structure 3 in. diameter by 1 in. thick of 1/8 in. cells with 0.002 in. wall thickness, is bolted to this reservoir. The honeycomb structure is painted with a black epoxy paint (Cat-A-Lac flat black, Finch Paint and Chemical Co.). The honeycomb radiator with this coating results in a theoretical emittance greater than 0.985. The radiator is provided with copper constantan thermocouples at various points to measure the temperature and effective isothermality of this body. Sliding vacuum seals were provided for both the radiator and the receiver support tubes so that the vertical positioning of the radiator and receiver surfaces could be readily changed during a test.

For the simulated solar radiation experiments, the radiator assembly was removed, and as indicated in Fig. 1b, a 6-in. diameter vycor window was placed directly below the calorimetric assembly. The radiation from a simulated solar source (Hanovia 537B1 Xenon-Mercury lamp is directed toward the receiver front surface by means of the optical system shown in the figure. A radiation calorimeter (Ref. 1) is mounted on a sliding-vacuum seal so that the intensity of the beam of simulated solar radiation can be monitored periodically during a test.

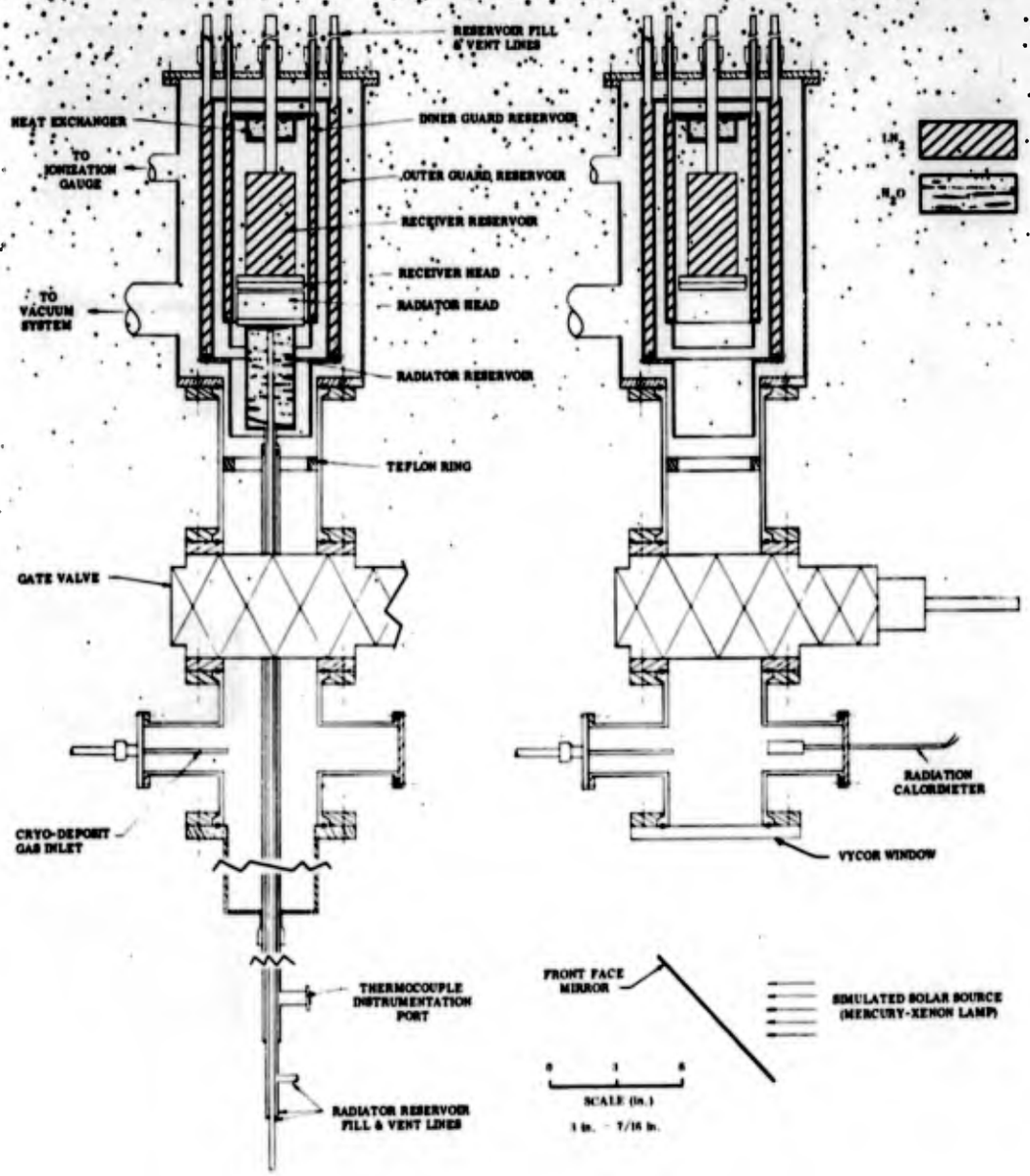

Fig. 1 Schematic of Calorimetric Portion of Experimental Apparatus

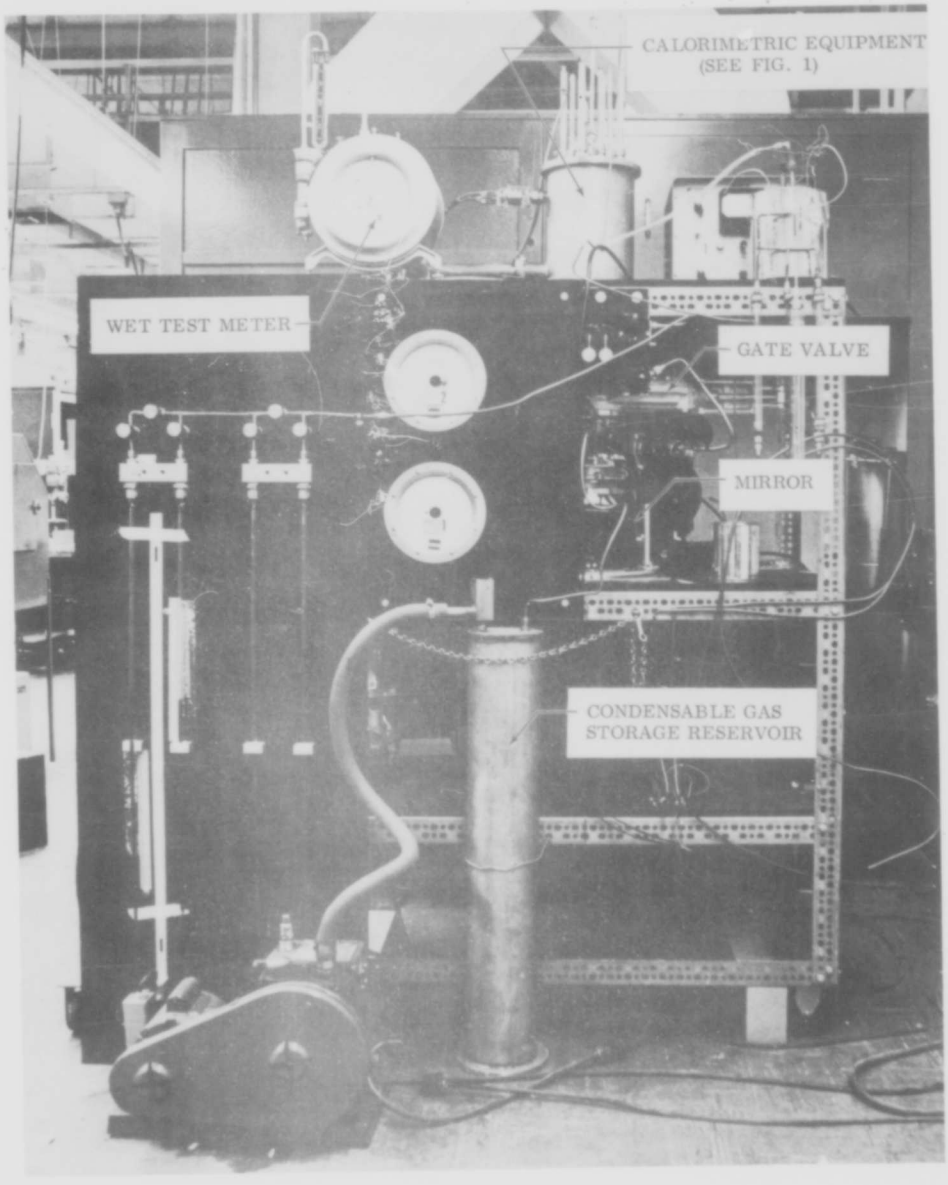

Fig. 2 Photograph of Calorimetric Apparatus

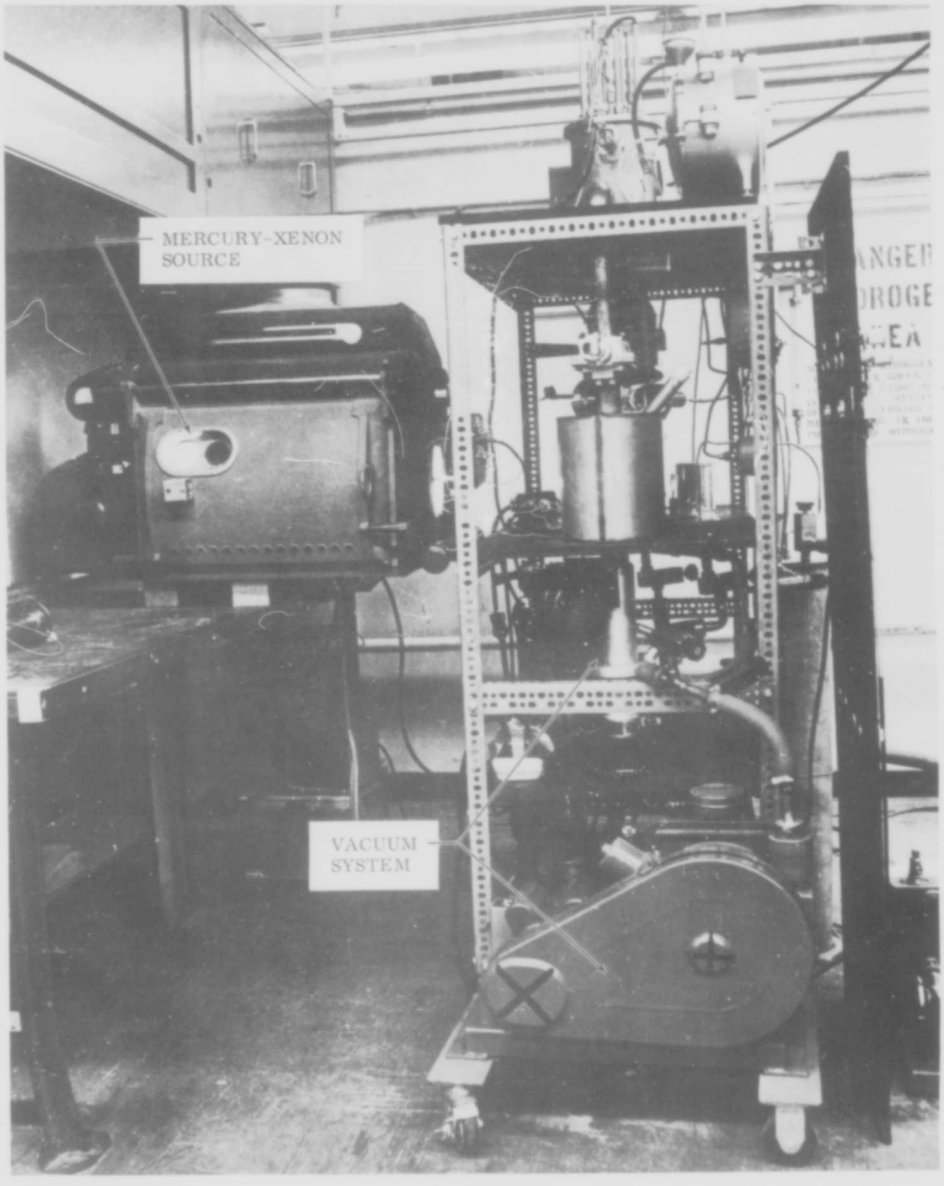

Fig. 3 Photograph of Calorimetric Apparatus With the Mercury-Xenon Source

The vacuum system, boil-off measuring equipment, and gas depositing system used with the total hemispherical radiation calorimeter are shown in Fig. 4. The vacuum system consists of a forepump (Welch 1402), a 2 in. oil diffusion pump (NRC 0148), and a liquid-nitrogen cold trap. The typical vacuum provided in the radiation calorimeter by this pumping system is about 5×10^{-6} Torr. The boil-off rate of liquid nitrogen from the receiver reservoir was measured by passing the nitrogen gas both through flow-rate meters (Predictability Flow-meters, Manostat Corp.) and total flow measuring equipment (Wet Test Meter, Precision Scientific Co.). These flow measuring devices were connected in series, and the gas flow rates measured by both methods were cross checked; they agreed to within 2%.* A heat exchanger was provided in the boil-off circuit to ensure that the nitrogen gas passing through the flow measuring equipment was at NTP. The gas depositing system used to produce the cryodeposits consisted of the vapor or gas source, a reservoir of known volume for storage of the gas to be deposited, pressure measuring devices, and flow metering equipment. The source of CO_2 was a commercial gas bottle; the source of the water vapor was a flask of distilled water.

The gas or vapor is introduced from its source via a valve into the reservoir. The total mass of gas deposited is calculated from the total pressure drop in the reservoir that occurs during the deposition process. The pressure drop is measured with both a manometer system and a differential pressure gauge (Wallace & Tiernan FA160 0-40 Torr); the initial pressure in the reservoir is measured with an absolute pressure gauge (Wallace & Tiernan FA129). For the water vapor deposition, the temperature of the vapor source was held lower than that of the rest of the gas deposition system to prevent condensation of the water vapor. (Condensation precludes using pressure measurements of the vapor in the reservoir as an accurate means of determining the mass of gas metered out of the system.) The gas metering system consists of a needle valve and a pressure gauge (NRC Alphatron Gauge) which is used to measure the gas-depositing pressure. The gas is injected into the depositing region through a tube shown in Fig. 1.

The condensate is observed by lowering first the radiator and then the receiver so that the front surface of the receiver is even with the lower surface of the teflon ring shown in Fig. 1. The section of the radiation calorimeter holding the teflon ring is made from 4 in. Pyrex pipe to permit observation of the film deposition and determination of its nature. A small probe on the face of the radiator contacts either the receiver face or the condensate deposited on the face. The thickness of this condensate is determined by measuring the difference in position of the radiator head when there is no deposit (i.e., the probe is in direct contact with the receiver face) to its position when there is a deposit on the receiver face. The teflon ring prevents gross escape of gas from the depositing region. Since the annular area between the teflon ring and the receiver is known, it is possible to calculate the fractional mass of gas which is not deposited on the front receiver surface.

*The final data in this report is based on the measurements made with the Wet Test Meter, since it is the more accurate of the two devices.

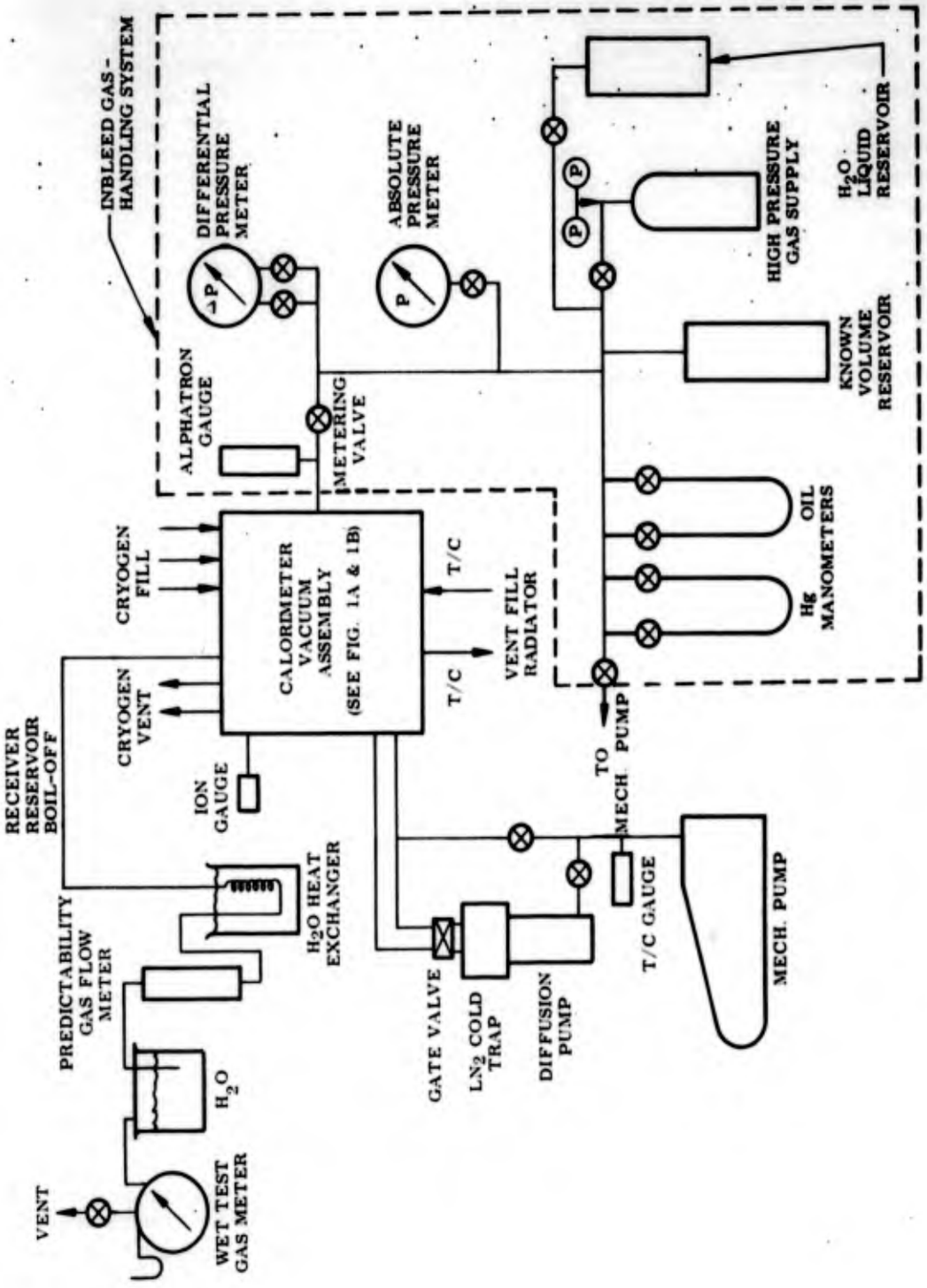

Fig. 4 Flow Diagram for the Experimental Absorptance Calorimeter

2.2 EXPERIMENTAL PROCEDURE

Before absorptance measurements of cryodeposits were made, the experimental apparatus was calibrated by mounting a honeycomb surface coated with Parsonaloid Optical Lacquer on the receiver reservoir. Thus, with two surfaces of known effective emittance (calculated from the analytic results), temperature, and separation, the theoretical heat exchange can be computed. Experimental measurements verified these results to within 2%. A more sensitive check for residual heat leaks to the receiver was accomplished by circulating liquid nitrogen through the radiator while the receiver contained liquid nitrogen. With the radiator at liquid-nitrogen temperature, the receiver boil-off was less than 1% of the 290°K blackbody to 77°K blackbody radiant heat exchange. The blackbody receiver head was also used to measure the intensity of the beam of solar simulated radiation; this result was then compared to the reading of the solar flux calorimeter to calibrate this calorimeter for its subsequent use of periodically checking the beam intensity of the simulated solar source.

Following calibration, the blackbody receiving surface was replaced by aluminum plates (2-7/8 in. in diameter) that were either polished or finished with Cat-A-Lac flat black epoxy paint. The absorptance of these surfaces without a cryodeposit was then determined.

To obtain a deposit of the condensable gas of interest, the radiator was lowered below the gas inlet port (see Fig. 1); next the receiver was lowered until its surface was flush with the teflon ring; the gas metering valve was opened. The depositing pressure, measured with an Alphatron gauge, was maintained at 4.6×10^{-4} Torr for water vapor and at 3.8×10^{-3} Torr for carbon dioxide. The resulting depositing rates on the receiver head were 0.014 lb/hr-ft^2 for water vapor and 0.188 lb/hr-ft^2 for carbon dioxide.

A recent investigation (Ref. 2) has shown that ice deposited on a 77°K substrate at pressures less than 5×10^{-3} Torr has an amorphous structure, while ice deposited at higher pressures has a cubic crystalline structure. The previously mentioned water vapor depositing pressure was chosen so that the resulting cryodeposit would be representative of that found in actual space simulation chambers.

2.3 RESULTS

The measured 300 to 77°K blackbody heat exchange agreed to within 2% of the theoretically predicted value. To check the radiator for diffuse emission, several separation distances for the radiator and receiver were used. Changing the radiator and receiver surfaces (3 in. diameter radiator, 2-7/8 in. diameter receiver) from a 1/16 to a 1/4 in. separation changes the theoretical diffuse radiation view factor from 0.90 to 0.81 (Ref. 3). The experimentally measured variation in radiant heat exchange due to these changes in separation agreed with energy interchange rates predicted theoretically on the basis of the above diffuse view factors to within the limits of experimental accuracy (2%). The results of these experiments indicate that the honeycomb radiator acts as a Lambertian surface.

Figure 5 shows that the infrared absorptance of water vapor condensed on a polished aluminum substrate increases very rapidly with thickness. At a thickness of only 4.5×10^{-5} in., the absorptance is 0.5. The agreement between the present data and the Douglas data (Ref. 4) used in Fig. 5, which was obtained with an equivalent source of radiation, and at a different receiver temperature (20°K), is not surprising. As stated by Kislovskii (Ref. 5), the optical constants of ice are only slightly changed in going from 263 to 77°K, and, from the nature of the dominating absorption bands in the infrared, it is expected that no change in optical properties would occur in going from 77 to 20°K. Figure 5 indicates that the water-vapor films are completely opaque to room-temperature energy at a thickness of approximately 0.01 in.

For 290°K radiation on a 77°K carbon dioxide film, the present data (Fig. 6) indicates that the films are quite transparent to infrared radiation. Opacity is not approached until film thicknesses exceed 0.1 in. As indicated in Fig. 6, the present data is in agreement with the Douglas data (Ref. 4), but is in disagreement with the ARO data (Ref. 6). This inconcistency probably results from difference in the nature of the deposits. The films deposited by ARO were most likely structurally transparent, since the snowy deposits obtained at their higher depositing pressures would be made up of isolated individual crystals. The films produced in our tests were dense and had the appearance of ice, (i.e., they were glassy and the substrate material could be observed through the films) which is typical of films deposited under rarified gas conditions.

The Mercury-Xenon source data for water-vapor films deposited on a 77°K substrate (Fig. 7) indicate that absorptance decreases with increasing film thickness. Although there is no other experimental data with which to compare the present data, the observed results are in qualitative agreement with the theoretical model that is described in the following section. The data indicate that a lower absorptance results when the source is filtered, and Fig. 8 indicates that the filtered source gives the better approximation of the extraterrestial solar spectral distribution. It should be noted that a deposit of significant thickness is required for a substantial decrease in system absorptance. A 0.02 in. film of water vapor on Cat-A-Lac Black (initial solar absorptance = 0.96, is required to reduce the system absorptance to 0.80.)

Without filter, the beam intensity of the simulated solar radiation was 3.5 suns. Initial runs with the intensity reduced to 0.5 suns indicated no change in absorptance values from those measured with 3.5 suns intensity. This result indicates that for simulated solar radiation intensity of at least up to 3.5 suns, the absorptance of 77°K water vapor films is independent of the intensity of the incident radiation flux.

It was found that with a clean substrate, the carbon dioxide and water vapor films firmly adhered to the substrate. However, when the polished aluminum substrate was covered with an oil film, not necessarily visible,* the films had a tendency to flake.

*The presence of a contaminating film can be inferred from higher than usual absorptance values for the polished substrate.

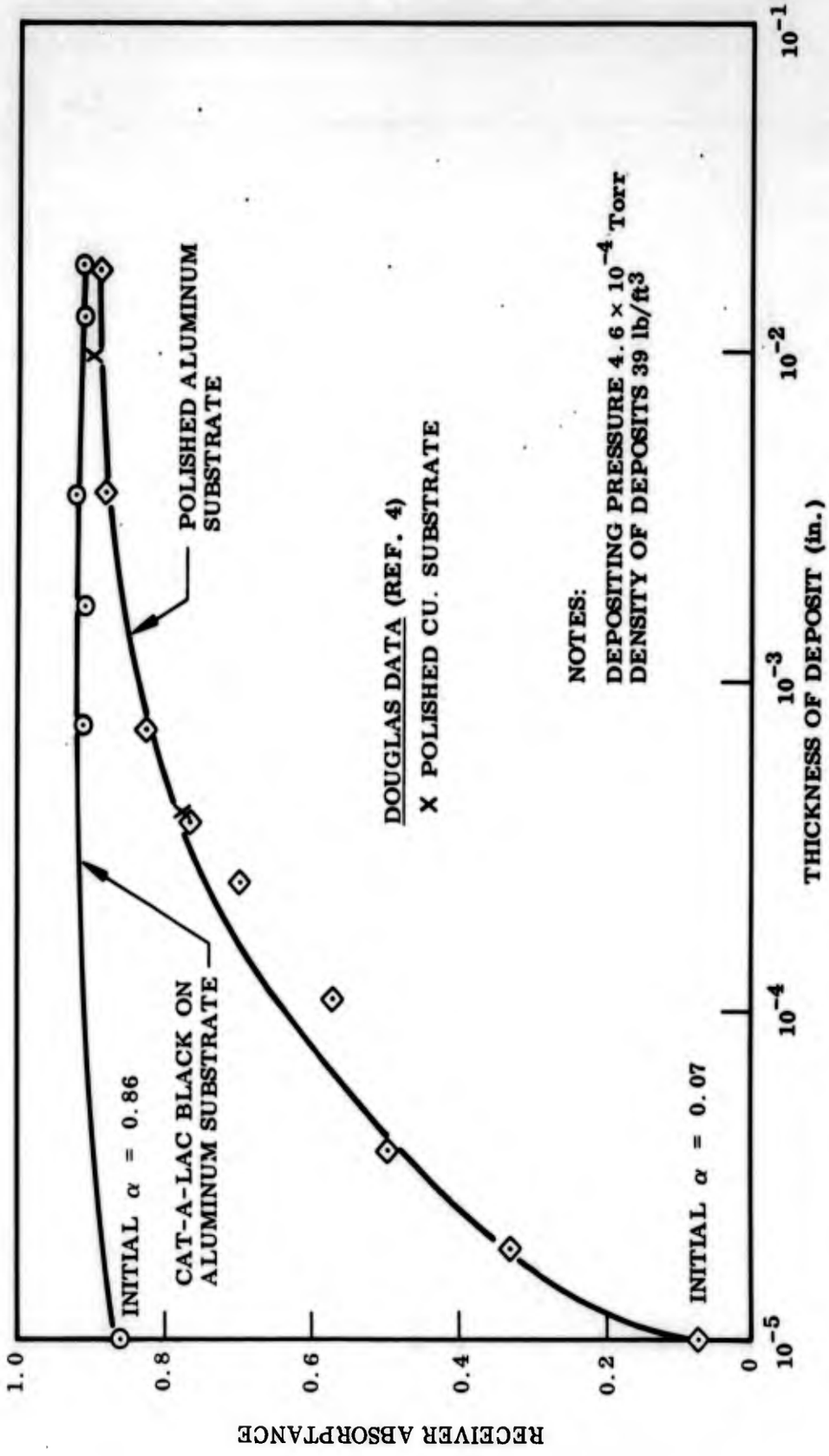

Fig. 5 Absorptance of H_2O Cryodeposit for Room Temperature Blackbody Radiation

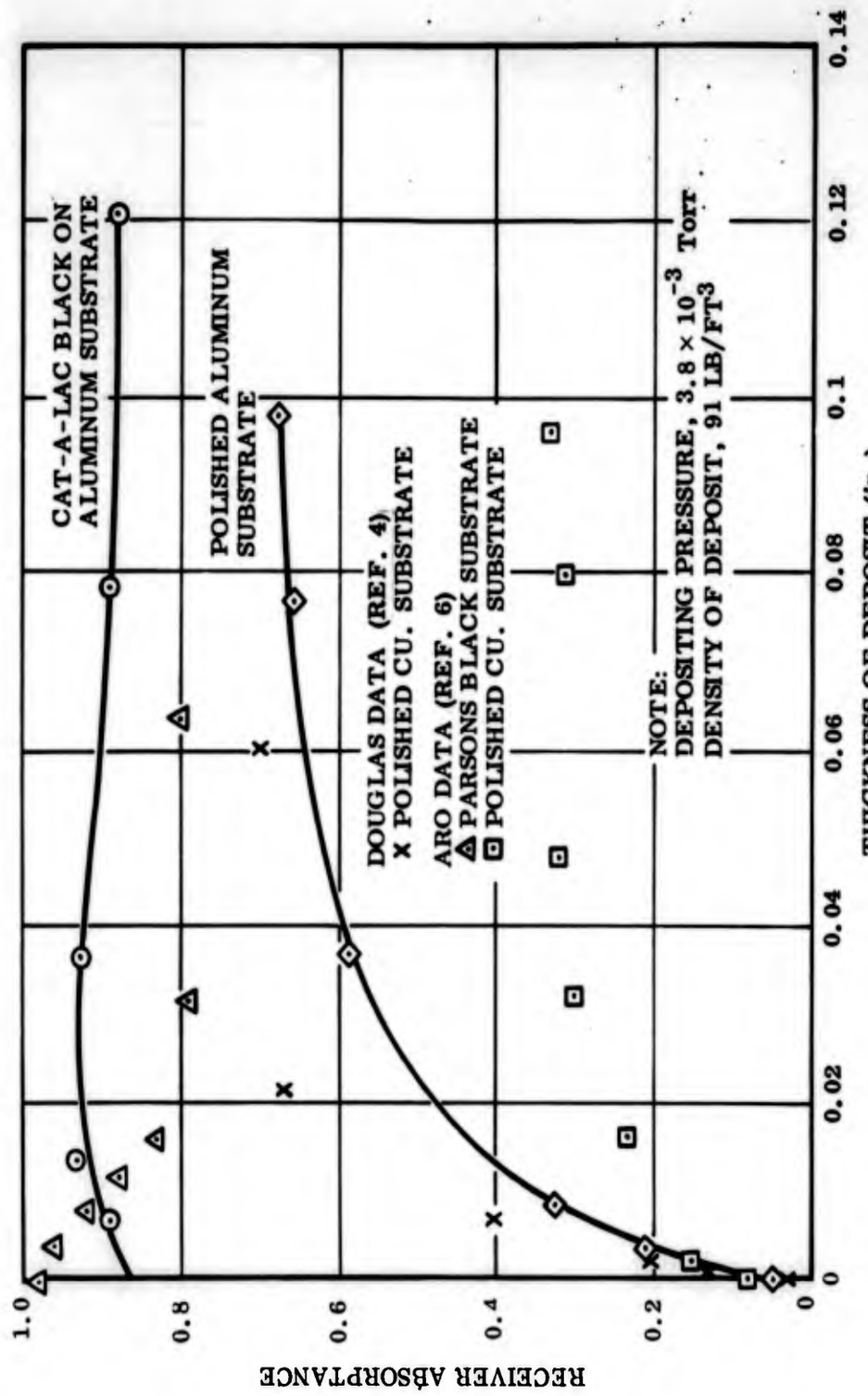

Fig. 6 Absorptance of CO_2 Cryodeposit for Room Temperature Blackbody Radiation

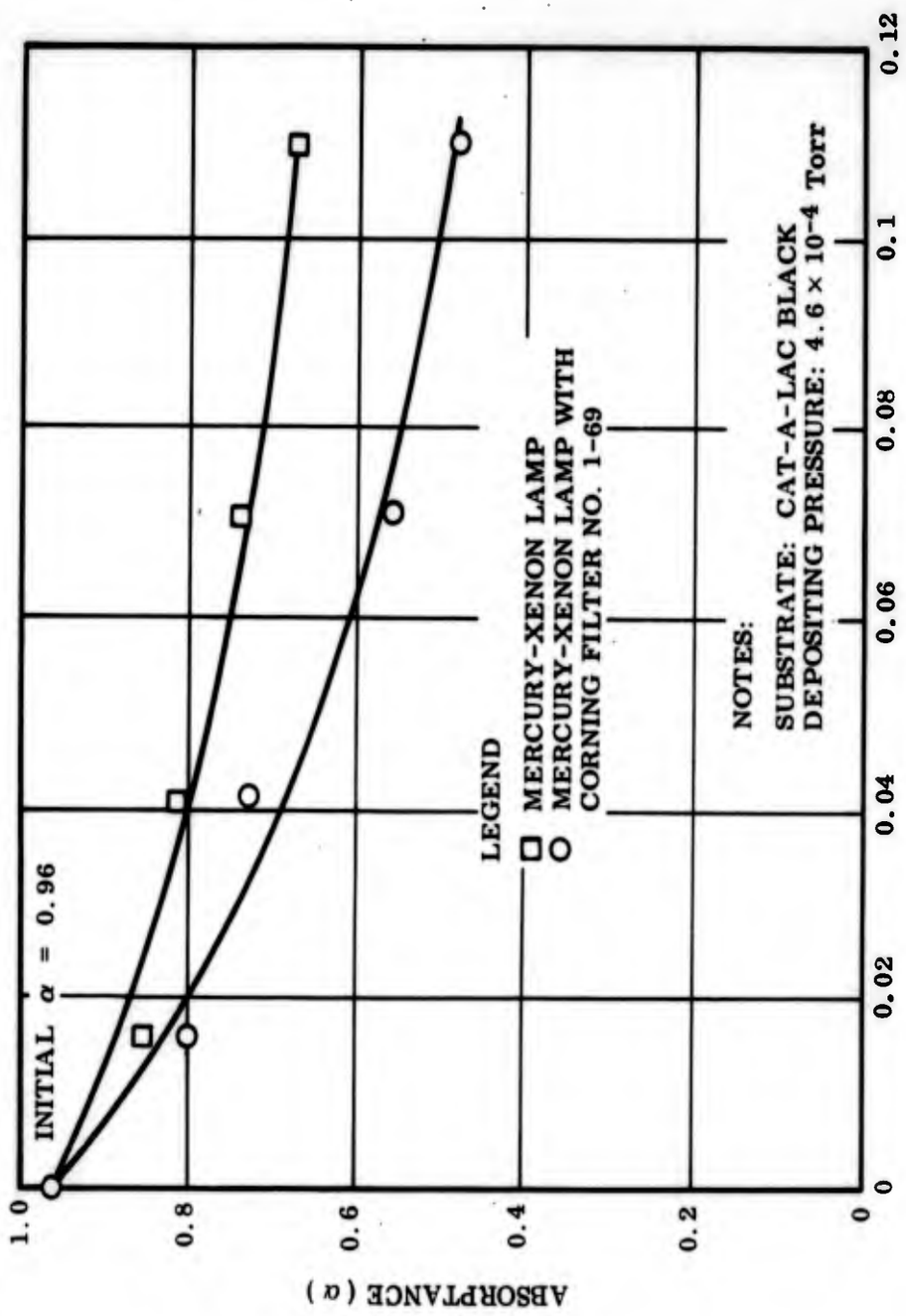

Fig. 7 Absorptance of H_2O Cryodeposit for Simulated Solar Energy

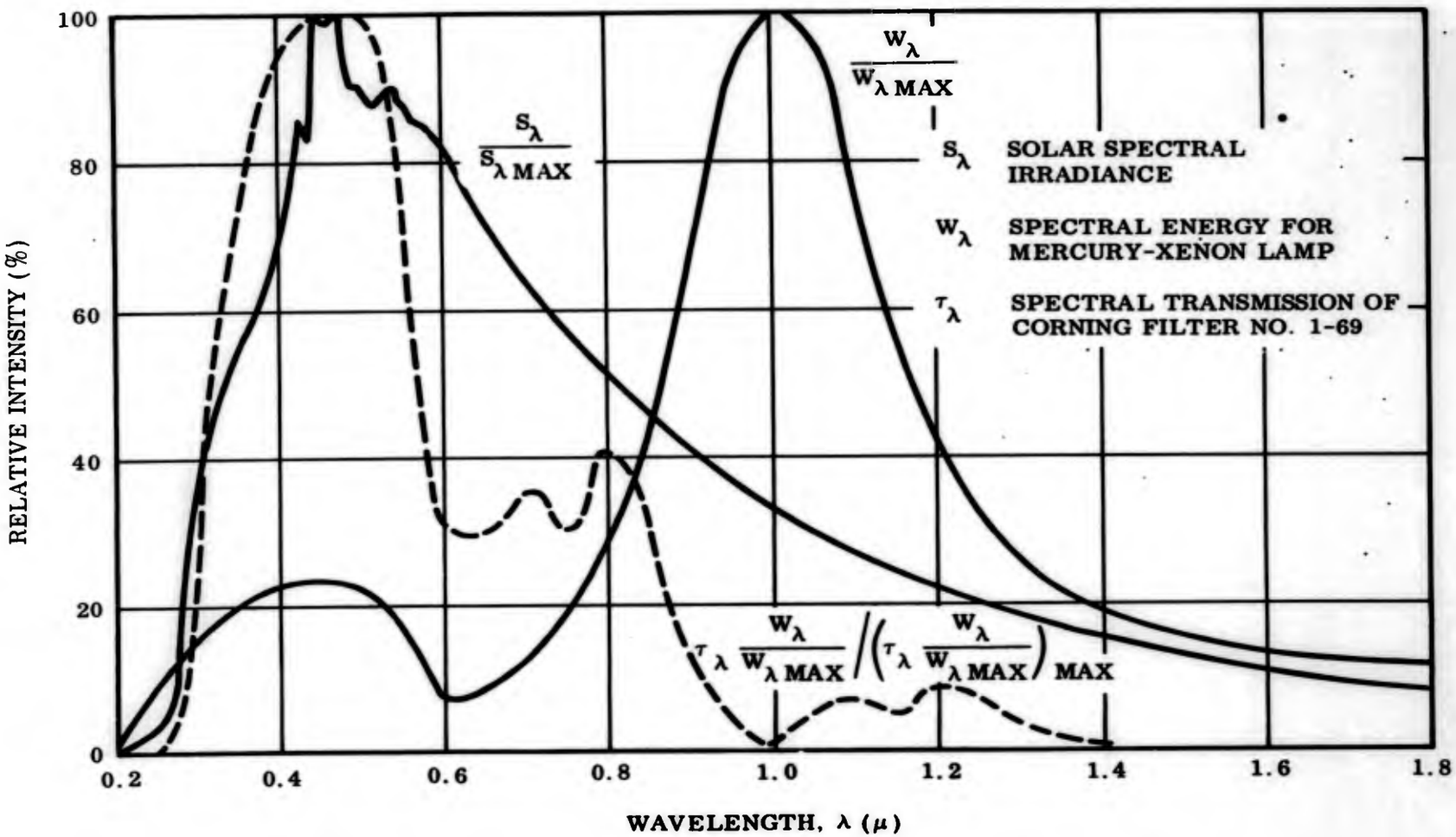

Fig. 8 Spectral Solar and Mercury-Xenon Lamp Energy Distribution

The measured densities of the cryodeposits were determined by measuring the condensate thickness that resulted from depositing a known mass of gas on the receiver. The measured densities ranged from 32 to 40 lb/ft^3 for water vapor and from 80 to 102 lb/ft^3 for carbon dioxide. The density of ice at 84°K is 58.4 lb/ft^3 as measured by Dewar (Ref. 7) and that of CO_2 is 104 lb/ft^3 at 90°K (Ref. 8). This data on ice and CO_2 at maximum density indicates that the deposits in the present experiments contained void volumes. This conclusion is also consistent with visual observations in the present experiment which indicated that the films were partially opaque – a phenomenon attributable to backscattering produced by the void volumes.

2.4 THEORY AND ANALYSIS OF RESULTS

Data on the optical absorption coefficient of ice (Ref. 9) in the visible and infrared wavelength region indicate that for the greater film thicknesses (>0.01 in.) used in the simulated solar radiation experiments, the radiation beyond 1.1μ will be totally absorbed, whereas the radiation having wavelengths less than 1.1μ will be almost totally transmitted. This, of course, neglects radiation reflected at the ice-vacuum interface. However, both visual observations and experimental density measurements show that a very large number of void volumes, which acted as scattering centers for the transmitted radiation, occurred in the ice films in the present experiments. These voids backscatter the radiation out of the ice film and thereby prevent its absorption at the Cat-A-Lac surface. The attenuation of the transmitted radiation caused by backscattering is of the form

$$I_b = \int I_\lambda \left(1 - e^{-k_\lambda x}\right) d\lambda$$

where

I_b is the intensity of the backscattered radiation
x is the film thickness
I_λ is the normalized radiation intensity per unit wavelength of the transmitted radiation, i.e., $\lambda < 1.1\mu$
k_λ is the scattering coefficient at wavelength λ

The total absorptivity of the ice-substrate system for an ice film of thickness x is thus given by the expression

$$A(x) = 1 - R - \int I_\lambda \left(1 - e^{-k_\lambda x}\right) d\lambda$$

where R is the reflection coefficient of the ice-vacuum interface. It is assumed here that there is negligible reflection at the substrate, as was the case in the present experiment in which the substrate absorptivity was 0.96. In the limit, as the film thickness becomes large so that

$$\int I_\lambda \left(1 - e^{-k_\lambda x}\right) d\lambda \rightarrow \int I_\lambda \, d\lambda$$

the absorptivity of the film will approach

$$A = 1 - R - F$$

where F is the fraction of the total radiation intensity in the transmitted region. The data presented in Fig. 7 is in agreement with the model discussed in this paragraph.

For the experiments involving 290°K blackbody radiation incident on a 77°K ice film, the optical constants of the ice in the wavelength region of interest can be calculated by means of the method developed by Kislovskii (Ref. 5). The optical constants in the infrared are the result of strong broad absorption bands centered about 3.2, 13, and 62 μ. These absorption bands give rise to a large extinction coefficient over the entire infrared region characteristic of a 290°K blackbody emitter. This high extinction coefficient is evidenced by the experimental data of Fig. 5.

For ice film thicknesses greater than 0.01 in., the spectral absorption coefficient measurements of Ockman (Ref. 9) indicate that practically all but the component of the 290°K blackbody radiation reflected at the ice-vacuum interface should be absorbed by the ice film. The data presented in Fig. 5 is consistent with the above results. Further, the reflection coefficient for the vacuum-ice interface was calculated for 290°K blackbody radiation by multiplying the normalized spectral distribution function for the radiation by the spectral reflection coefficient, which was calculated with the aid of the derived optical constants. This calculation gives a reflection coefficient of 0.07, which is in close agreement with the data shown in Fig. 5.

The major absorption bands occurring in CO_2 in the infrared are at 2.7, 4.3, 15, and 100 μ (Refs. 10 and 11). These bands are so narrow and weak that solid CO_2 can be considered to be highly transparent in the infrared. The data on solid CO_2 films shown in Fig. 6 is consistent with a model of a film with an absorption coefficient having an average value of 8 cm^{-1} (it is interesting to compare this with the value of 600 cm^{-1} for ice in the corresponding wavelength region) and a vacuum-carbon dioxide film reflection coefficient of 0.10.

Section 3

ABSORPTANCE OF 20°K DRY AIR, N_2, AND CO_2 FILMS FOR 77°K BLACKBODY RADIATION

3.1 EXPERIMENTAL APPARATUS

The experimental equipment shown in Fig. 1 and used for the liquid nitrogen temperature experiments proved to be unsatisfactory for the liquid-hydrogen temperature work. It was found that the heat leak down the boiloff tube was several times the 77°K to 20°K blackbody heat exchange. The apparatus was modified by thermally shorting the boiloff tube about three inches above the boiloff reservoir to the liquid hydrogen guard chamber and by placing a liquid nitrogen heat exchanger inside the top of the boiloff tube. The boiloff tube was entirely vacuum jacketed to the top and covered with aluminum foil so that it would have a low absorptance. These modifications were introduced to intercept all thermal energy conducted down the boiloff tube, prevent convection currents in the hydrogen gas venting up the boiloff tube, and to reduce all radiation loads on the boiloff reservoir. Extra radiation shielding was also placed where the radiator is introduced through the openings in the guard chambers. It was still found after all these modifications were made that the total heat leaks to the boiloff reservoir were greater than 2×10^{-2} watts whereas the anticipated 77°K to 20°K blackbody radiation transfer was about 10^{-2} watts. It was therefore decided to use the apparatus shown in Figs. 9 and 10 for the studies of the absorptance of 20°K cryodeposits for 77°K blackbody radiation. This apparatus had just been completed for other experiments planned at LMSC. The apparatus essentially consists of a three-inch diameter 77°K extended surface blackbody and a three-inch diameter polished aluminum receiver cooled to 20°K by thermal contact with a reservoir containing liquid hydrogen. The radiator is cooled by thermal contact with the liquid-hydrogen bath through low thermal-conductance supports and is heated to the desired radiator temperature by means of joule heating of resistors imbedded in the radiator. The temperature of the radiator is determined with a platinum resistance thermometer mounted on the radiator. This platinum resistance thermometer has been calibrated by N.B.S. for the temperature range between 10° and 90°K. The rate of boiloff of the liquid hydrogen in the receiver is then used to measure the total energy absorbed by the receiver. The hydrogen reservoir has two lines connected to it; one line serves as the liquid hydrogen fill line while the other line is connected to the equipment used to monitor the hydrogen boiloff rate. The radiator, receiver, and the four-inch sections of the reservoir fill and boiloff lines are enclosed in a vacuum space whose outer walls are immersed in a liquid hydrogen bath. The liquid hydrogen temperature walls of the vacuum enclosure serve to thermally isolate the receiver from all its surroundings except for the radiator. The pressure over the hydrogen guard bath is maintained several inches of water higher than that over the liquid hydrogen in the boiloff reservoir. This pressurization prevents the hydrogen that leaves the reservoir volume from condensing in the fill and boiloff lines while it passes through the hydrogen bath.

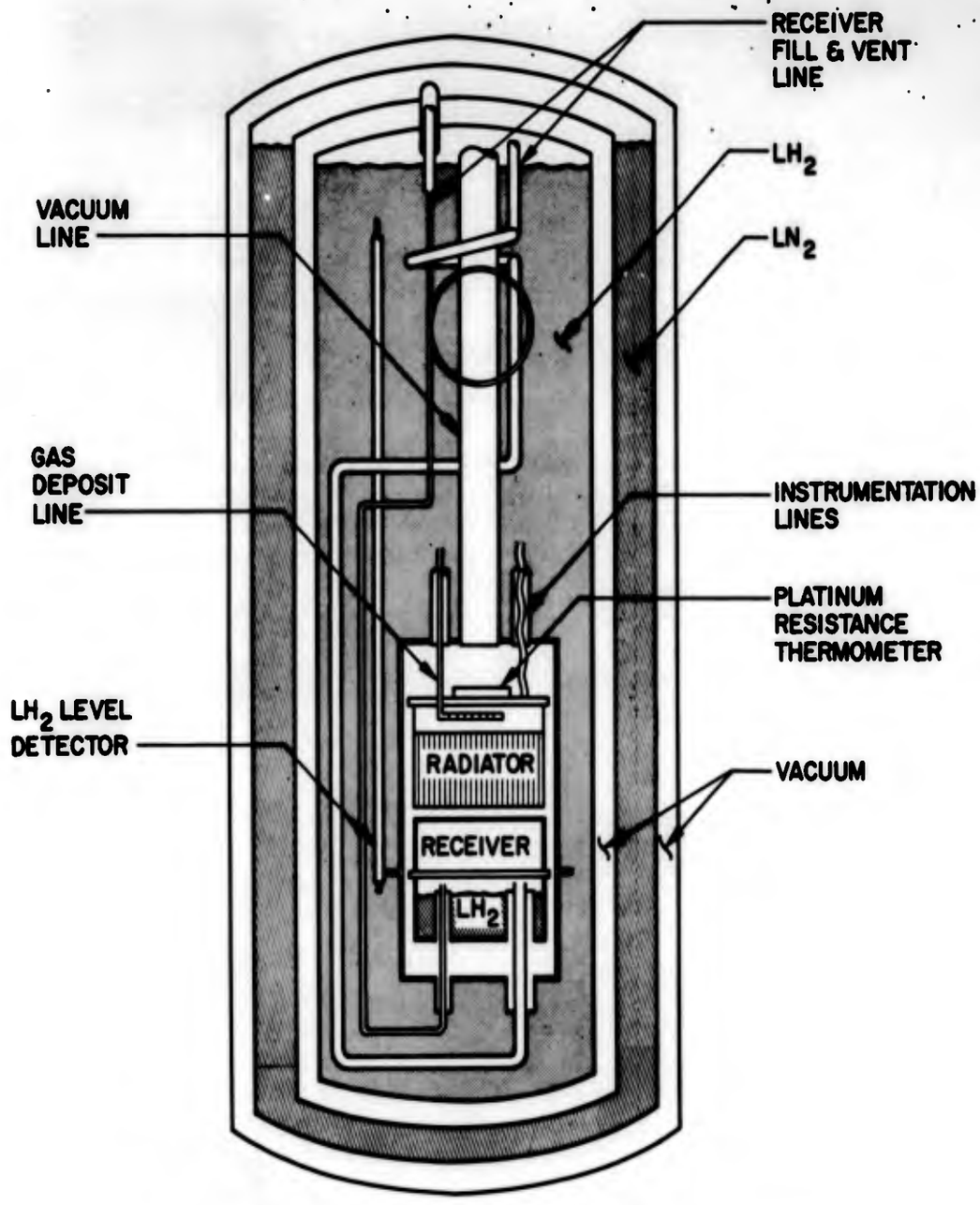

Fig. 9 Schematic of Low-Temperature Absorptance Calorimeter

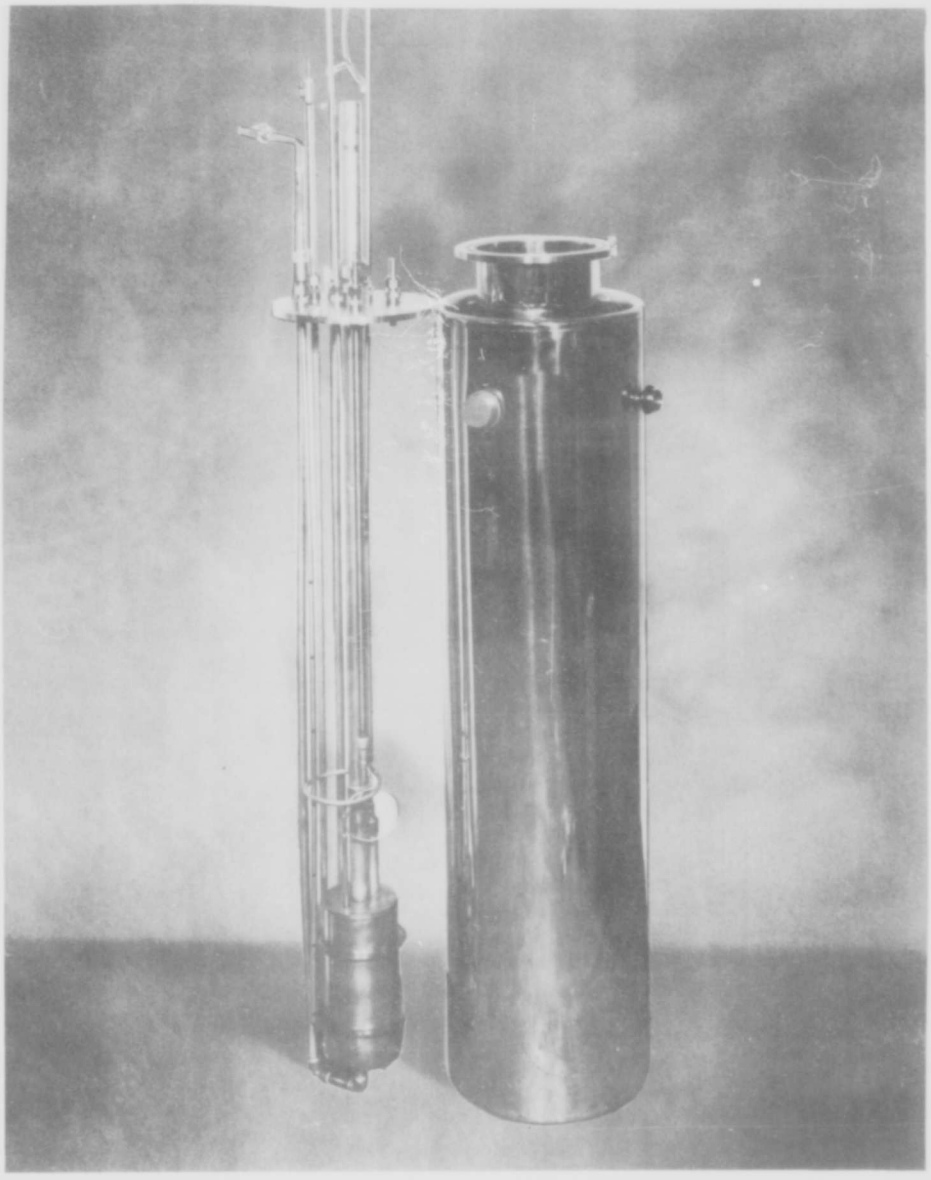

Fig. 10 Photograph of Low-Temperature Absorptance Calorimeter

In these experiments, the boiloff rates of the hydrogen gas at NTP to be measured ranged from approximately 0.01 to 0.25 cm^3/sec. The boiloff in these experiments was measured by allowing the hydrogen gas to pass through a U tube filled with soap solution and then measuring the rate at which the successive horizontal soap films moved up an accurately graduated tube. The tube was made from a 10 ml pipette. Typically, the successive soap films were spaced about 1 cm apart. A precision wet-test meter in series with the pipette device was used as a double check.

The vacuum in the apparatus was maintained with the liquid nitrogen-trapped two-inch oil diffusion pump system used for the 77°K experiments. The pressure measured in the line going to the apparatus was typically 5×10^{-7} torr with no liquid hydrogen in the apparatus. With liquid hydrogen in the apparatus, the gas pressure in the experimental volume was undoubtedly below 10^{-9} torr except during the time of depositing. Since at pressures below 10^{-6} torr residual gas conduction in the experimental volume is unimportant, we may conclude that residual gas conduction is of no consequence in the present apparatus. The apparatus is evacuated through a one-inch diameter thin-wall stainless tube which passes through the hydrogen bath as is shown in Fig. 10. The radiator also serves as a means of uniformly depositing the films of interest onto the polished aluminum receiver. The gas to be condensed is metered down an 1/8-in. diameter vacuum-jacketed tube into the apparatus that uses the gas metering equipment shown in Fig. 4. The gas passes out of the tube into a volume in the radiator 3 in. in diameter by 1/2 in. high. This volume is located between the radiator back plate and the backface of the brass tubes which constitute the blackbody radiator. These tubes are 1-1/2 in. long, 5/16 in. O.D., and are tapered to a knifeedge at the front surface; they are closely packed and soldered into a 3-in. O.D. copper tube. The front edge of the brass tubes are flush with the front edge of the 3-in. diameter copper tube, thus creating the volume into which the depositing gas is metered. Since tubes with these characteristic dimensions have a low conductance for gas at rarified pressure, the gas metered into the volume behind the tubes passes out of the tubes uniformly over the front surface of the radiator. The 20°K receiver is directly opposite the front surface of the radiator and hence the gas is uniformly deposited on the receiver. The array of brass tubes is painted with CAT-A-LAC flat black paint, and with their high M'/W ratio, they provide good blackbody radiation. During the film-depositing process, the radiator and gas-depositing line are heated to a temperature above their characteristic condensation temperature to prevent condensation of the depositing gas in this part of the system. The heating of the radiator is accomplished with joule heating of carbon resistors, while the gas deposit line is heated by means of joule heating of a nicrome-wire spiral wrapped down this structure.

3.2 EXPERIMENTAL PROCEDURE

A three-inch diameter CAT-A-LAC coated honeycomb blackbody receiver is used to calibrate the apparatus. When this receiver is in place, the dewar containing the apparatus and the receiver reservoir are filled with liquid hydrogen, and the radiator is brought to temperature. The boiloff from the reservoir is checked from time to time until the apparatus comes to steady state ($\simeq$ 4 hr) and several steady-state boiloff readings are taken.

After the calibration, the vacuum chamber was broken open by grinding off one of the heli-arced joints and a polished aluminum receiver was substituted for the blackbody receiver. The receivers are bolted onto the receiver reservoir for easy removal. The experimental procedure with the polished aluminum receiver in place is the same as outlined above for the blackbody receiver. After several boiloff readings are taken, gas deposition begins. Note that for the low gas-flow rates involved in these experiments, over 12 hr are required for each reading of the wet-test meter. Thus an entire run of several gas deposits, involves a 48 to 72-hr time span.

The gas is deposited by means of the same equipment used for the 77°K deposition work (Fig. 4). The gas-depositing line is vacuum jacketed where it passes through the hydrogen bath to prevent condensation of the depositing gas in the line. Even with vacuum jacketing, the line still cools enough radiatively in the 12 to 24 hours between deposits to freeze the depositing gas and thereby block this line. Thus, the inner tube is wrapped with heater wire and warmed by joule heating as previously stated.

The liquid hydrogen used in these experiments was checked for orthohydrogen concentration to insure that no errors would occur due to orthohydrogen-parahydrogen conversion.

3.3 RESULTS

The experimentally measured 77°K blackbody to 20°K blackbody heat-transfer rate agreed to within 3 percent of the analytically predicted values. During the calibration, the radiator temperature was varied from 70°K to 150°K and the measured heat-transfer rate followed the T^4 dependence to within 3 percent. Thus extraneous heat leaks presented no problem.

For a CO_2 film deposit of about 90 mils, the measured total absorptance (based on an assumed density of 91.4 lb/ft^3 as measured in the 77°K film work) was 0.118; absorptance of the substrate before depositing was 0.075. Thus the increase in absorptance due to the CO_2 film was approximately 0.04.

In the case of N_2 and air, the measured total absorptance of films approximately 70 mils thick (based on an assumed solid density of 60 lb/ft^3) was 0.092; the absorptance of the substrate before deposition was 0.075. Thus the increase in absorptance due to the air and N_2 films was approximately 0.02.

The high initial absorptance of the aluminum substrate (Ref. 12) is believed to be caused by the system contaminants, oil and/or water vapor. For 77°K radiation, then, this large initial absorptance may present greater engineering problems than are presented by the cryodeposits.

3.4 THEORY

The experimental results on the 20°K CO_2 films are in agreement with the work of previous investigators (Refs. 10 and 11). Their results, which are based on the transmittance and reflectance of CO_2 films, show that the only absorption bands of interest, for

work with 77°K blackbody radiation are at 15 and 100μ. These two bands are narrow and weak and hence CO_2 films should show little absorptance for 77°K blackbody radiation as evidenced in the present results.

Measurements (Refs. 13 and 14) made on the infrared transmittance of solid nitrogen and oxygen films with temperatures down to 34.4°K in the wavelength range from 2.5 to 25μ indicate that these films are almost totally transparent. Solid oxygen has only one weak absorption band occurring at 6.4μ in this wavelength range, while solid nitrogen has one weak absorption band at 4.2μ. At wavelengths greater than 25μ, a single absorption band associated with the lattice vibrational frequency should appear in both solids. Thus for 77°K blackbody radiation, both solid nitrogen, oxygen, and hence solid air, should be highly transparent. The results of the present experimental measurements indicate that this is indeed the case.

Section 4
ANALYTICAL DETERMINATION OF THE EFFECTIVE EMITTANCE OF EXTENDED SURFACE GEOMETRIES

4.1 INTRODUCTION

To simulate the thermal radiation sink qualities of space, a test vehicle must be surrounded by a shroud with highly absorbing walls that radiate and reflect very little energy. When the shroud is cooled to a temperature in the range of 80 to 100°K, the thermal energy emitted to the vehicle by the shroud can be reduced to less than a fraction of a percent of the thermal energy emitted by the vehicle. The walls of the shroud must be highly absorbent in order that little of the solar simulation flux and of the thermal energy emitted by the test vehicle will be reflected back to the vehicle. No paint systems exist that have a high enough absorptance to produce this behavior when applied to a shroud with smooth walls. Extended surfaces present a method of providing the desired absorptances approaching unity. The purpose of this portion of the report is to determine analytically the effective emittance of two extended surface configurations which may be employed as shrouds in space simulation chambers. The extended surface geometries studied are the honeycomb configuration and the serrated V-groove. These particular geometries were chosen because they are the most practical and are commercially available.

The effective emittance of an extended surface configuration is defined as the ratio of the energy which actually leaves the configuration to the energy which, at the same temperature,would leave a blackbody plane having the dimensions of the projected area of the configuration. The assumption is made that all surfaces are isothermal, possess gray-body characteristics, and emit and reflect diffusely; i.e., according to a Lambertian cosine distribution. From Kirchhoff's law, it can be shown that the effective absorptance is equal to the effective emittance for the same angular distribution of energy.

To calculate the effective emittance of an extended surface configuration, it is necessary to determine

- The radiosity (emitted plus reflected energy) as a function of local surface position
- The portion of this energy which escapes from the configuration

The infinitely long V-groove configuration is amenable to integration. As a result, the radiosity can be determined exactly as a function of local surface position; the energy leaving the configuration can also be determined exactly. Other geometrical configurations, such as a honeycomb, are not amenable to an exact solution. In such cases, the configuration may be divided into a finite number of smaller surfaces and the radiosity determined for each, the radiosity being assumed constant over each surface element. The greater the local surface emittance, the less important multiple reflections become with the result that a more uniform radiosity is obtained. However, since the radiosity, in general, does vary over the surface of the configuration, greatest accuracy can be achieved by breaking the configuration into as many small elements as possible.

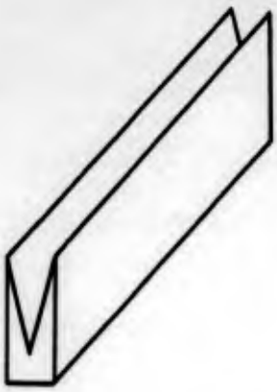

Fig. 11 V-Groove Configuration

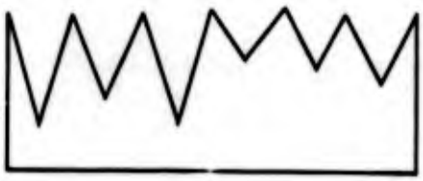

Fig. 12 Series of V-Grooves

Fig. 13 Serrated V-Groove Configuration

4.2 EFFECTIVE EMITTANCE OF THE V-GROOVE CONFIGURATION

The V-groove configuration under consideration is shown in Fig. 11. It is assumed that the groove is infinitely long so that end effects may be neglected. Once the effective emittance of a single V-groove has been determined, the effective emittance of a series of V-grooves physically joined to one another (Fig. 12) can be determined. The effective emittance of such a configuration is the area-weighted average of the effective emittance of the individual grooves.

Some of the existing V-groove configurations are serrated with smaller V-shaped grooves along the major groove legs (Fig. 13). An estimate of the effective emittance of such a configuration may be made as follows. The smaller grooves may be analyzed first and the effective emittance of each determined. The angular distribution of energy from each of these grooves can be determined and compared with that from a Lambertian surface. It is found that the energy leaving each smaller groove is nearly distributed according to the cosine law;* the serrated surface may be considered to be a flat Lambertian surface having the previously determined value of emittance. The effective emittance of the major groove may now be determined by means of the newly obtained value of emittance for the serrated legs.

The significant portions of an analysis to determine the effective emittance of a long V-shaped groove are presented below. The detailed analysis is given in Appendix C. The groove and the co-ordinates employed are shown in Fig. 14.

*This holds for groove apex angles of approximately 110 deg – the typical angle of commercially available serrated V-grooves.

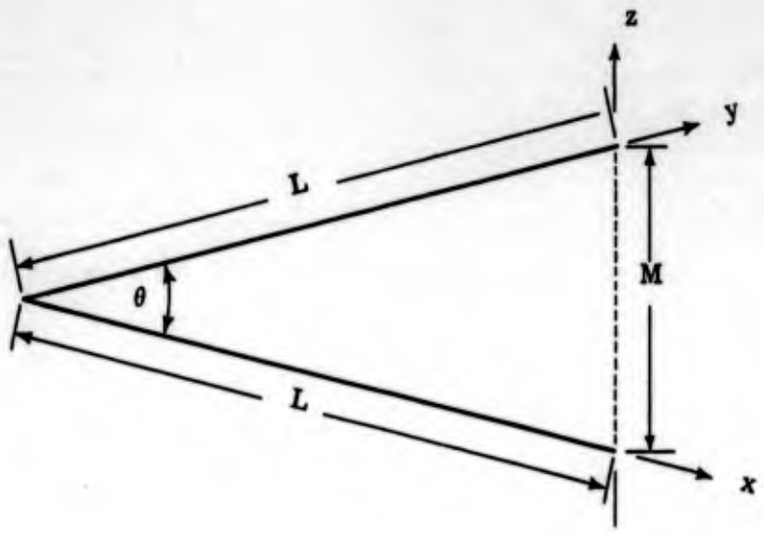

Fig. 14 V-Groove Co-ordinates

The total radiant flux (emitted plus reflected radiant energy) leaving a position x on one leg of the V-groove is

$$B(x) = \epsilon \sigma T^4 + \rho H(x) \tag{4.1}$$

The term $H(x)$ which represents the energy leaving leg y that impinges upon unit area of leg x at position x, is (Ref. 15):

$$H(x) = \frac{1}{2} \int_{y=0}^{L} B(y) \frac{xy(1 - \cos^2 \theta)\, dy}{\left(x^2 + y^2 - 2xy \cos \theta\right)^{3/2}} \tag{4.2}$$

Substituting Eq. (4.2) into Eq. (4.1) results in

$$B(x) = \epsilon \sigma T^4 + \frac{\rho(1 - \cos^2 \theta)}{2} \int_{0}^{L} B(y) \frac{xy\, dy}{\left(x^2 + y^2 - 2xy \cos \theta\right)^{3/2}} \tag{4.3}$$

which in dimensionless form can be written

$$\beta(X) = 1 + \frac{\rho(1 - \cos^2\theta)}{2} \int_{Y=0}^{1} \beta(Y) \frac{XY\,dY}{\left(X^2 + Y^2 - 2XY\cos\theta\right)^{3/2}} \tag{4.3a}$$

Since physical symmetry exists, $B(x) = B(y)$ and $\beta(X) = \beta(Y)$; thus, the solution of Eq. (4.3) or (4.3a) provides the radiosity.

It is now possible to determine $H(z)$, the flux leaving the groove opening, and H_T, the total energy leaving the groove. In dimensionless form, $\bar{H}(Z) = H(z)/\epsilon\sigma T^4$ was determined to be (see Appendix C)

$$\bar{H}(Z) = \frac{1}{2} \int_{X=1}^{0} \frac{\beta(X)Z(X - 1)(1 - \cos^2\psi)\,dX}{\left[Z^2 + (1 - X)^2 - 2Z(1 - X)\cos\psi\right]^{3/2}}$$

$$+ \frac{1}{2} \int_{X=1}^{0} \beta(X) \frac{(\bar{M} - Z)(X - 1)(1 - \cos^2\psi)\,dX}{\left[(\bar{M} - Z)^2 + (1 - X)^2 - 2(\bar{M} - Z)(1 - X)\cos\psi\right]^{3/2}} \tag{4.4}$$

The total energy leaving the groove is

$$H_T = \int_{z=0}^{M} H(z)\,dz \tag{4.5}$$

which in dimensionless form becomes

$$\bar{H}_T = L \int_{Z=0}^{\bar{M}} \bar{H}(Z)\,dZ \tag{4.5a}$$

The effective emittance is

$$\epsilon_{eff} = \frac{H_T}{M\sigma T^4} = \frac{\epsilon}{\bar{M}} \int_{Z=0}^{\bar{M}} \bar{H}(Z)\, dZ \tag{4.6}$$

Eqs (4.3a), (4.4) and (4.6) were programmed and numerically solved with an IBM 7090 computer. The solutions are in parametric form, the parameters being the groove apex angle and the local surface emittance. The apex angle was varied from 15 to 120 deg in various increments, while the local emittance was varied from 0.1 to 0.98. Resultant values of the V-groove effective emittance are plotted in Fig. 15; these results can also be more generally represented in the form of a quadratic equation. The coefficients of this equation are presented in Figs. 16, 17, and 18. For V-groove apex angles between 15 and 30 deg and for local emittances greater than 0.3, the values given by the quadratic equation are accurate to within approximately 4 percent of the computer solution. For lower θ and ϵ values, there are problems with the convergence of the computer solutions for B(x) because of a singularity in this function. By making an analytic expansion about the singularity in B(x), it was possible to derive an analytic expression for ϵ_{eff} which holds for $\theta < 5$ deg and $\epsilon > 0.2$. This expression is as follows:

$$\epsilon_{eff} = 1 + \frac{1}{2}\left(1 - \frac{1}{\epsilon}\right)\theta^2 \tag{4.7}$$

where θ is in radians.

For $\epsilon > 0.3$ and $5 < \theta < 15$ deg an extrapolation must be made between the results given by the above expansion for $\theta < 5$ deg and the results given by the equation given in Figs. 16, 17, and 18.

As has been mentioned, the effective emittance of a serrated V-groove configuration can be estimated if it can be determined that the energy leaving the small serrations is approximately distributed according to the cosine law. Once this fact has been established, it is only necessary to replace the serrated surfaces with Lambertian surfaces (Fig. 13) having the emittance of the small serrated V-grooves. From Fig. 19, it is seen that when the angle of sighting is within the apex angle, i.e., $\tau \leq \theta/2$, the mean radiation per unit solid angle per unit projected area of surface in that direction is

$$r_1 = \frac{\int_0^L \frac{B(x)}{\pi} \sin\left(\frac{\theta}{2} - \tau\right) dx + \int_0^L \frac{B(x)}{\pi} \sin\left(\frac{\theta}{2} + \tau\right) dx}{2\, L \sin\frac{\theta}{2} \cos\tau} \tag{4.8}$$

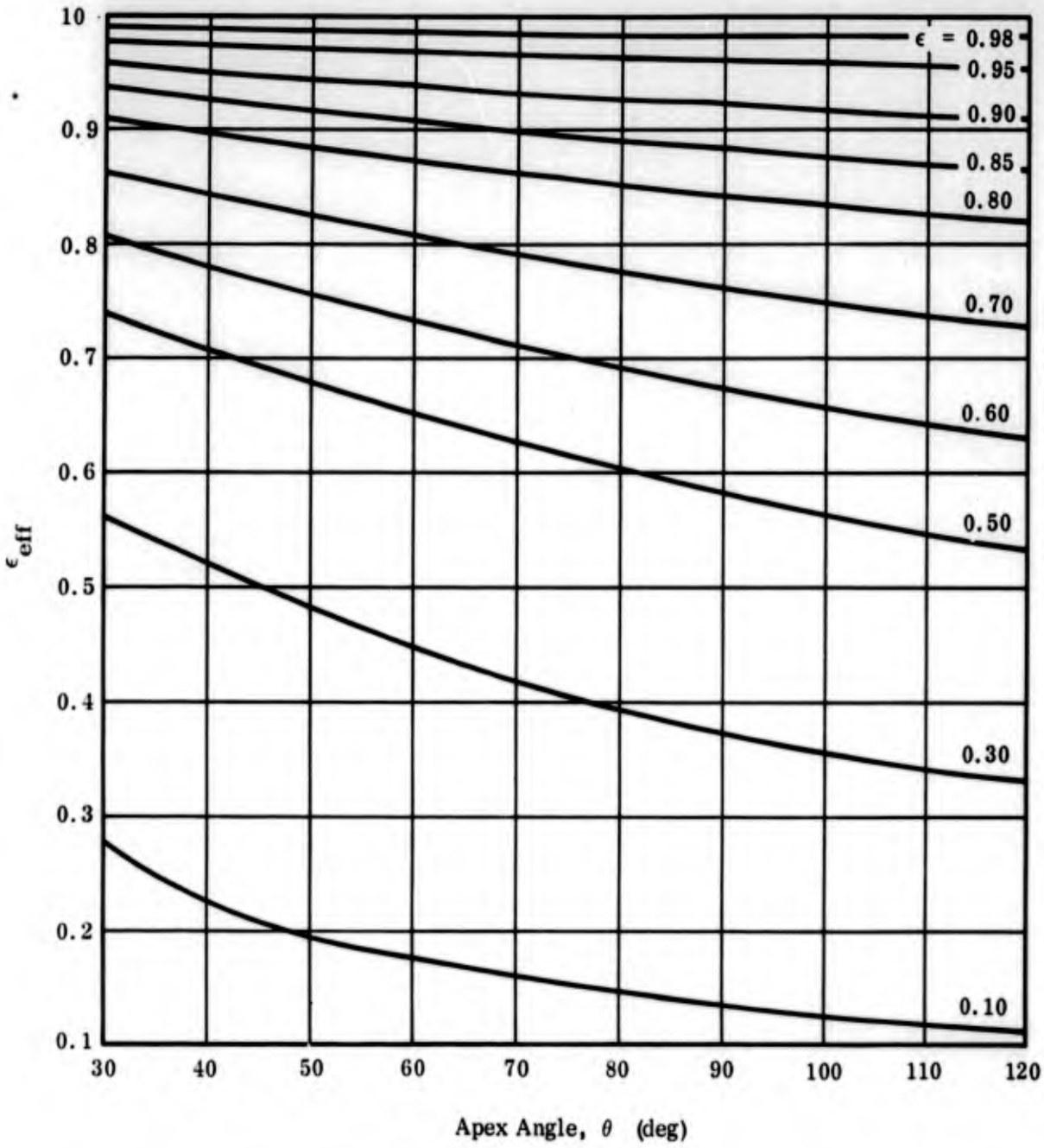

Fig. 15 Effective Emittance of a V-Groove as a Function of Apex Angle and Local Surface Emittance

VALUE OF C_1 TO BE USED IN THE EQUATION

$$\epsilon_{eff} = C_1 - C_2\theta + C_3\theta^2$$

Where ϵ_{eff} = Emittance of V-Groove

θ = Apex Angle in Deg

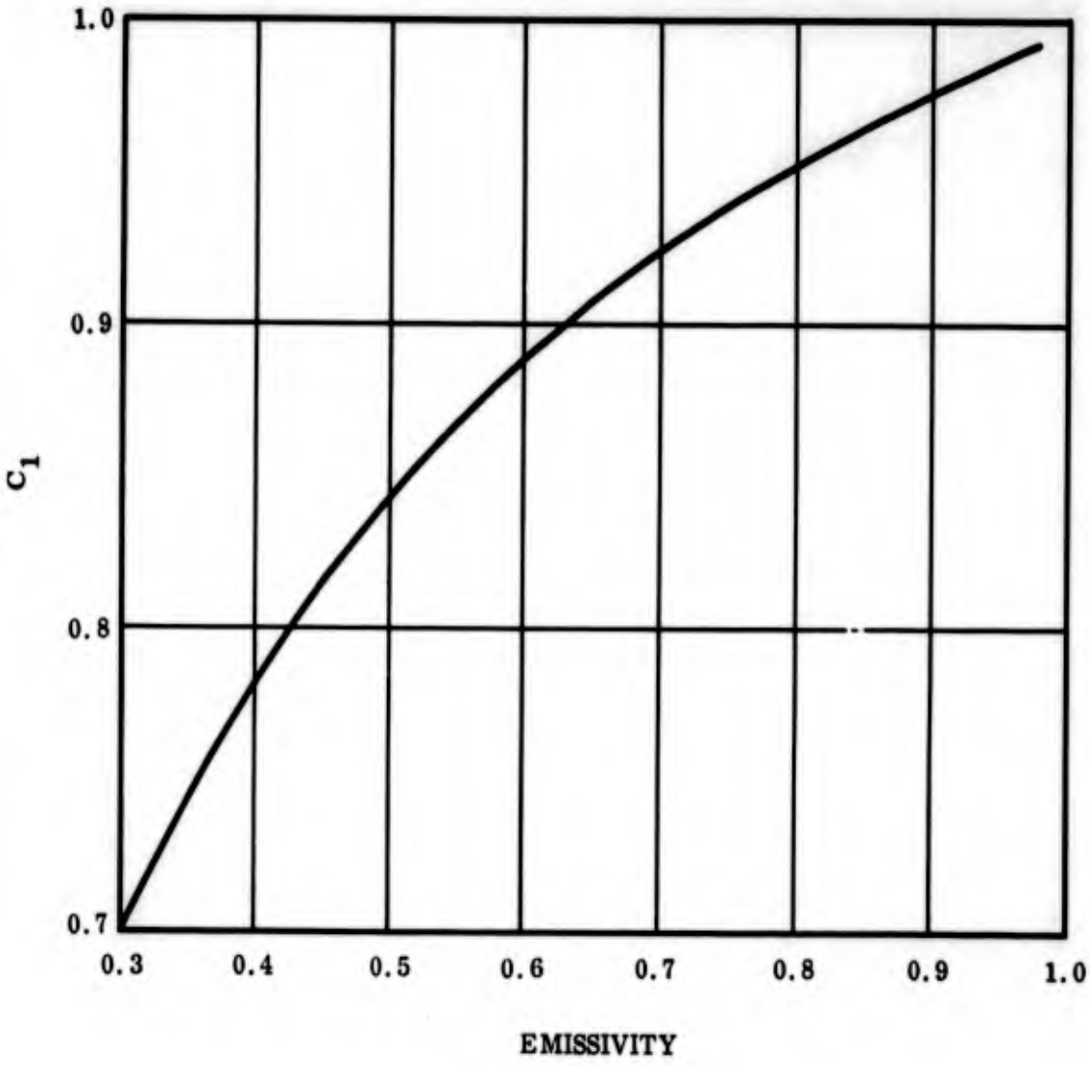

Fig. 16 Value of C_1 to be Used in the V-Groove Effective Emittance Equation

VALUE OF C_2 TO BE USED IN THE EQUATION

$$\epsilon_{eff} = C_1 - C_2\theta + C_3\theta^2$$

Where ϵ_{eff} = Emittance of V-Groove

θ = Apex Angle in Deg

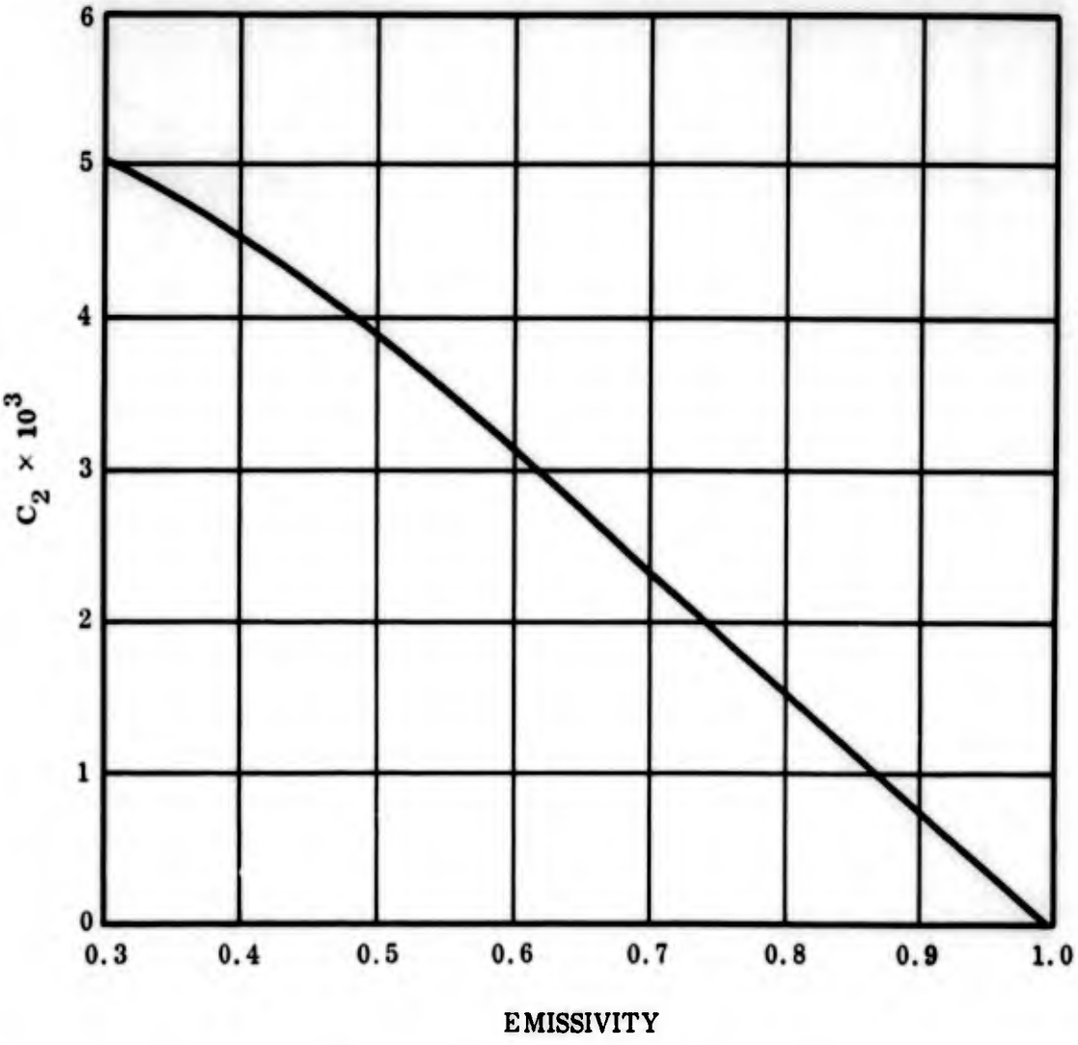

Fig. 17 Value of C_2 to be Used in the V-Groove Effective Emittance Equation

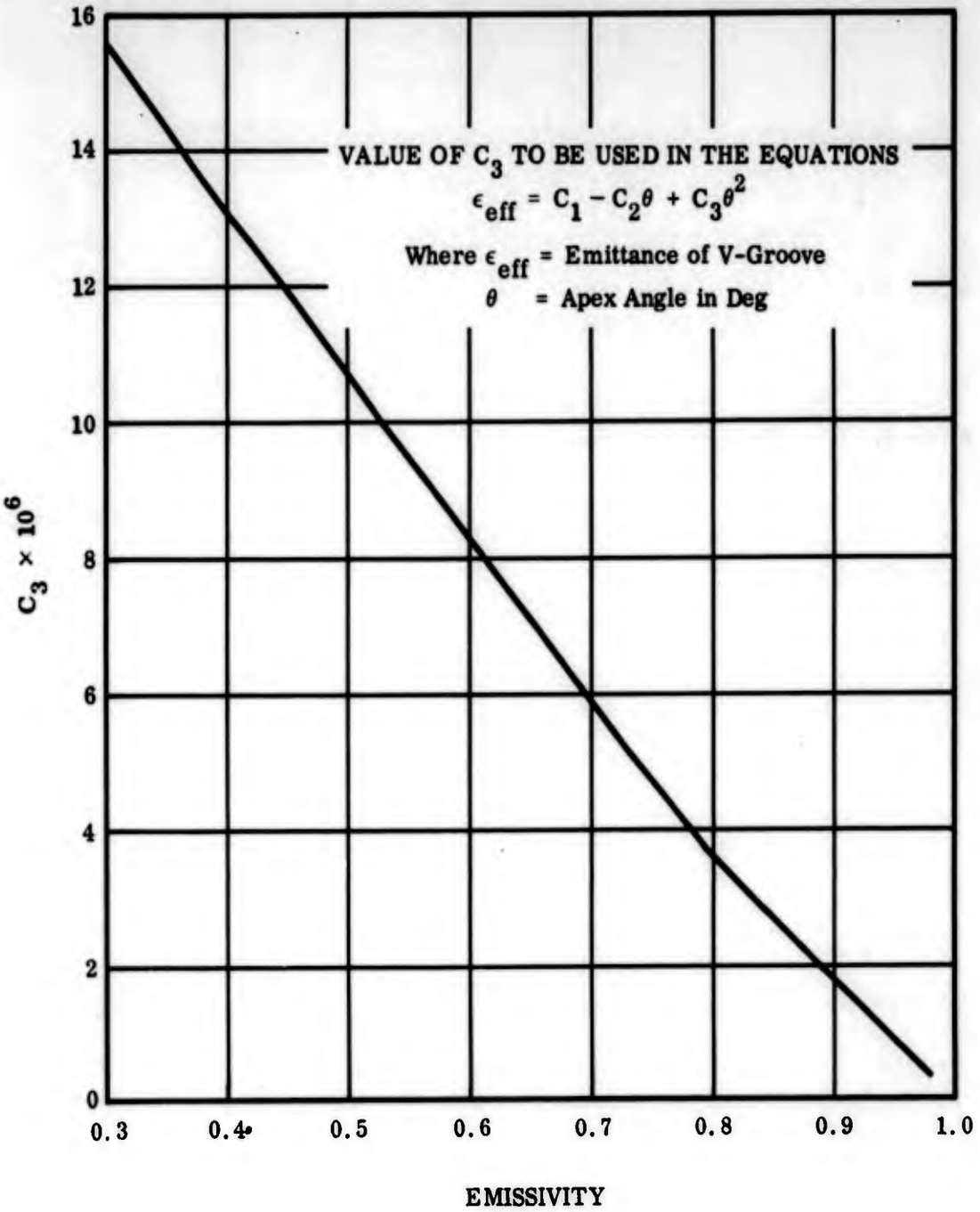

Fig. 18 Value of C_3 to be Used in the V-Groove Effective Emittance Equation

Fig. 19 V-Groove – Showing Angle of Sighting

which can be written

$$r_1 = \frac{\sin\left(\frac{\theta}{2} - \tau\right) + \sin\left(\frac{\theta}{2} + \tau\right)}{2\,L\,\pi \sin\frac{\theta}{2}\cos\tau} \int_0^L B(x)\,dx \qquad = \frac{1}{L\pi}\int_0^L B(x)\,dx \tag{4.8a}$$

in dimensionless form, Eq. (4.8a) becomes

$$R_1 = \frac{1}{\pi}\int_0^1 \beta(X)\,dX \tag{4.8b}$$

Since Eq. (4.8b) is independent of θ, the energy is distributed according to the cosine law when the angle of sighting is within the apex angle (Ref. 16). When the angle of sighting τ is not within the apex angle, i.e., $\tau > \theta/2$

$$r_1 = \frac{1}{2\pi L \sin\frac{\theta}{2}\cos\tau}\int_b^L \sin\left(\frac{\theta}{2} + \tau\right) B(x)\,dx \tag{4.9}$$

$$b = \frac{L \sin\left(\tau - \frac{\theta}{2}\right)}{\sin\left(\tau + \frac{\theta}{2}\right)}$$

in dimensionless form Eq. (4.9) becomes

$$R_1 = \frac{1}{2\pi \sin\frac{\theta}{2}\cos\tau}\int_B^1 \sin\left(\frac{\theta}{2}+\tau\right)\beta(X)\,dX \qquad B = \frac{\sin\left(\tau-\frac{\theta}{2}\right)}{\sin\left(\tau+\frac{\theta}{2}\right)} \qquad (4.9a)$$

Thus, in order to accurately estimate the effective emittance of a serrated V-groove geometry by assuming the replacement of the serrated walls by a Lambertian surface having the same effective emittance as the walls, the apex angle of the serrations must be large. Otherwise, the foregoing analysis will yield an effective emittance for the complete geometric arrangement which is on the low side of the actual value. Thus for surfaces of practical interest, i.e., serrated V-grooves for space chamber shrouds, the geometry is such that a conservative solution for the effective emittance results. That is, the effective emittance calculated will be lower than the actual effective emittance.

4.3 EFFECTIVE EMITTANCE OF THE HONEYCOMB CONFIGURATION

The honeycomb configuration under consideration is shown in Figs. 20 and 21. There is only one opening per cell through which radiant energy can escape. Since all cells of the configuration are identical, only one cell is considered (Fig. 21).

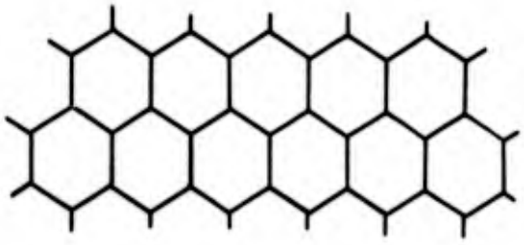

Fig. 20 Honeycomb Panel Configuration

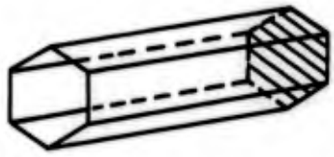

Fig. 21 Honeycomb Cell

To calculate the effective emittance of a honeycomb cell, the energy which actually leaves the configuration must be determined. The simplest approach involves the solution of a two-node Oppenheim network (Ref. 17). The two-node analysis is admittedly inaccurate for low surface emittances and/or high cell length to opening ratios. However, the results of a more refined analysis (seven-node solution) and the comparison of the two-node solution for cylindrical cavities with the exact solution for cylindrical cavities are included to show that the two-node solution for honeycomb is sufficiently accurate for determining the effective emittance of panels of practical interest.

Before proceeding, a brief description of the Oppenheim method is outlined. This method presumes that the surfaces are gray, i.e., α and ϵ are independent of wavelength, and that the surfaces emit and reflect diffusely. For finding the net radiation heat transfer between isothermal surfaces, an analogous electrical circuit is utilized. For a two-surface (or node) system, the circuit is given by

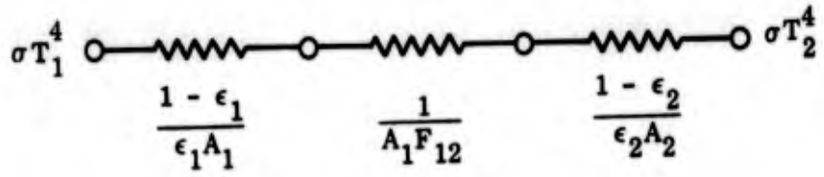

For a three-surface (or node) system, the circuit is given by

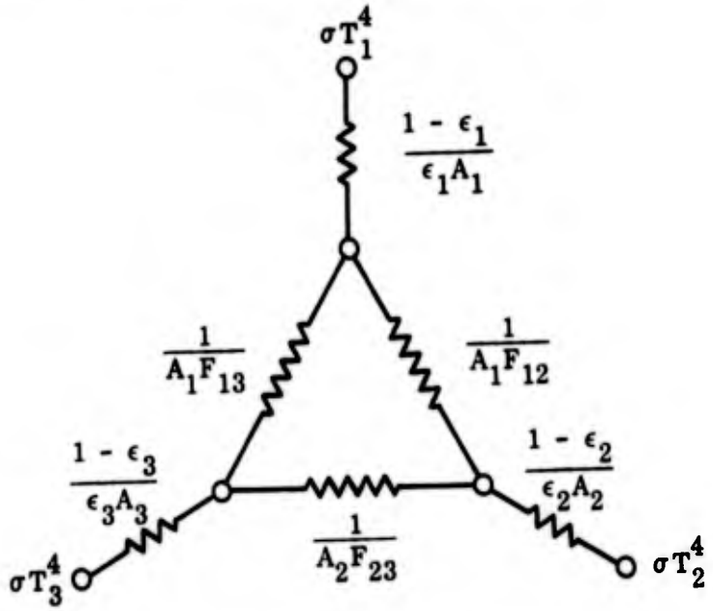

The σT^4 values correspond to the voltages or potentials of the circuit, and the resistances are as indicated. The net radiant heat transfer between nodes is given by solving for the current flow between nodes. For the two-node problem, the current is given by

$$I = \frac{V_1 - V_2}{\Sigma R_E} \tag{4.12}$$

where I is equivalent to the net radiation heat transfer. Thus

$$q_{1-2} = \frac{\sigma T_1^4 - \sigma T_2^4}{\frac{1 - \epsilon_1}{\epsilon_1 A_1} + \frac{1}{A_1 F_{12}} + \frac{1 - \epsilon_2}{\epsilon_2 A_2}} \tag{4.13}$$

If in the honeycomb configuration, surface 1 is considered to be a hypothetical black plane at the cell opening and surface 2 constitutes the total inside area of the cell, then

$$F_{12} = 1 \qquad \text{and} \qquad \epsilon_1 = 1$$

and Eq. (4.13) reduces to

$$q_{1-2} = \frac{A_1\left(\sigma T_1^4 - \sigma T_2^4\right)}{1 + \frac{A_1}{A_2}\left(\frac{1}{\epsilon_2} - 1\right)} \tag{4.14}$$

To find ϵ_{eff} of the honeycomb cavity, replace the cavity with a surface that is parallel to and the same size as A_1 and equate the heat transfer for the two situations.

Thus,

$$q_{1-2} = \frac{A_1\left(\sigma T_1^4 - \sigma T_2^4\right)}{1 + \frac{A_1}{A_2}\left(\frac{1}{\epsilon_1} - 1\right)} = \frac{A_1\left(\sigma T_1^4 - \sigma T_2^4\right)}{\frac{1}{\epsilon_{eff}}} \tag{4.15}$$

Therefore

$$\epsilon_{eff} = \frac{1}{1 + \frac{A_1}{A_2}\left(\frac{1}{\epsilon_2} - 1\right)} \tag{4.16}$$

where $\epsilon_2 = \epsilon$ = local emittance of the honeycomb surface. The results of the above calculation for various honeycomb configurations are plotted in Fig. 22.

To check the accuracy of the simplified two-node approach, the effective emittances of cylindrical cavities were computed and compared to an exact integral solution that is available in the literature (Ref. 18). Additionally, the effective emittances of cylindrical cavities were computed by using a three-node Oppenheim network. The results of the above analyses are included in Table 1.

Table 1

EFFECTIVE EMITTANCES OF CYLINDRICAL CAVITIES

Cylinder Length to Diameter Ratio	Surface Emittance								
	$\epsilon = 0.5$			$\epsilon = 0.75$			$\epsilon = 0.90$		
	Method of Solution								
	E	3N	2N	E	3N	2N	E	3N	2N
0.25	0.657	0.662	0.667	0.849	0.853	0.857	0.943	0.946	0.947
1	0.808	0.833	0.833	0.923	0.937	0.938	0.972	0.978	0.978
4	0.837	0.944	0.945	0.932	0.981	0.981	0.975	0.994	0.994

NOTE: E refers to exact solution
3N refers to three-node solution
2N refers to two-node solution

Table 1 indicates that the approximate solutions are sufficiently accurate when the surface emittances are high ($\epsilon \geq 0.75$), regardless of the cylinder length-to-diameter ratio. However, for a given surface emittance, the approximate solutions become increasingly inaccurate as the cylinder length-to-diameter ratio increases. Also, for a fixed length-to-diameter ratio, the approximate solutions become increasingly inaccurate as the local surface emittance decreases. However, it should be reemphasized that the two-node solution for the honeycomb effective emittance is sufficiently accurate for the purpose of designing space chamber honeycomb shrouds. This reasoning is supported by calling attention to the following practical considerations:

1) To provide adequate thermal simulation, a space chamber shroud should have a high effective emittance. Other desirable requirements include a minimum amount of thermal mass and isothermal surfaces. If honeycomb were to be used as the shroud material, the combined requirements mentioned above would dictate the use of a local high-emittance surface coupled with a low length-to-opening ratio. Fortuitously, this is the region where approximate analyses are accurate. Additionally, unless the surfaces are gray, i.e., α and ϵ are independent of wavelength, the analysis for effective

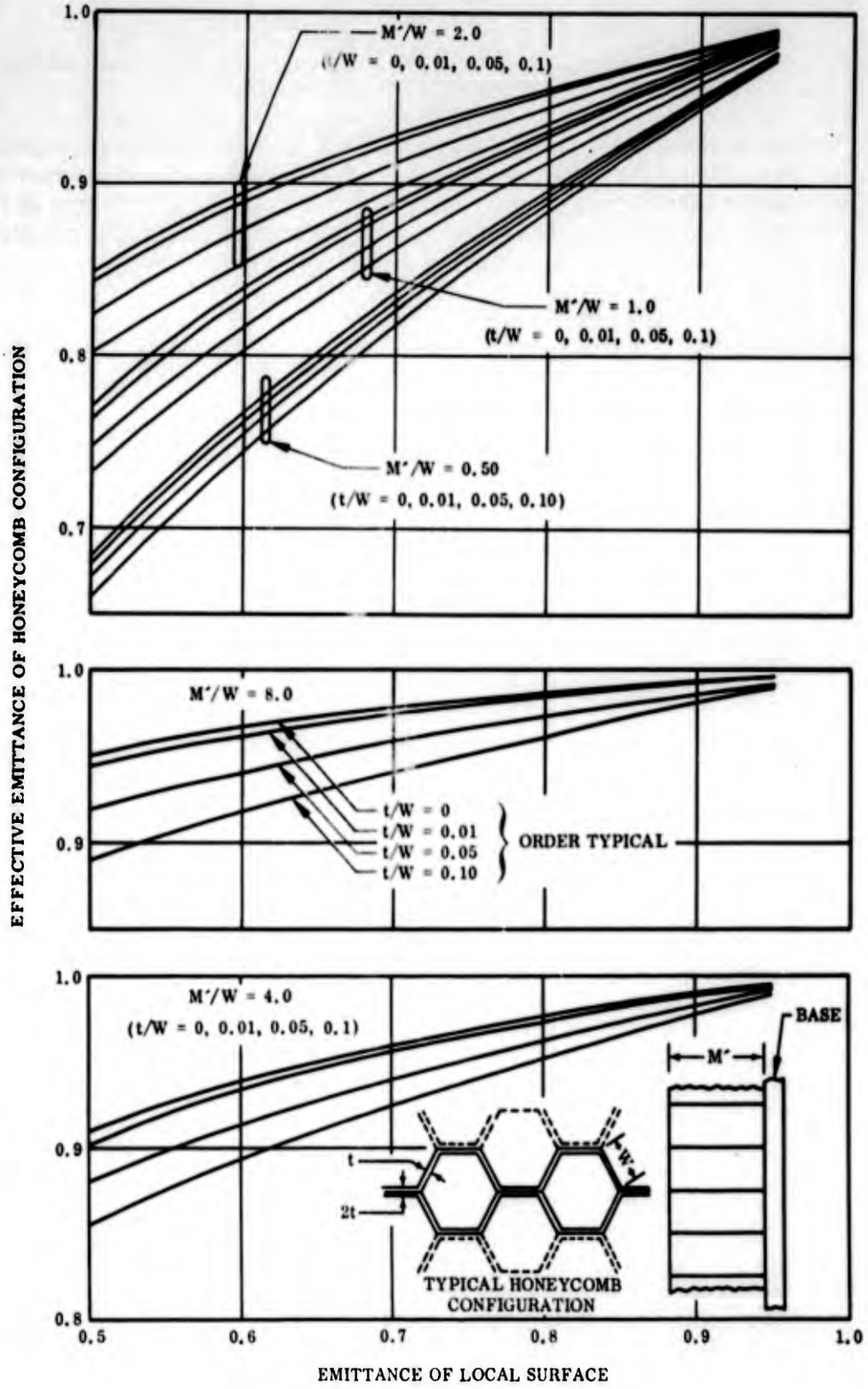

Fig. 22 Effective Emittance of the Honeycomb Configuration

emittance (or absorptance) becomes, in a practical sense, impossible. It should be mentioned that the only practical shroud coatings that are gray in both the visible and infrared regions are visibly dark dielectrics, and hence the coating emittance is high.

2) The experimental results found elsewhere in this report indicate that the cryodeposits of practical interest either have a high transmittance and/or a high absorptance in the infrared region. Therefore, the addition of these cryodeposits to a high-emittance dialectrically coated substrate will not invalidate the accuracy of the approximate solution where the incident radiation is in the infrared region.
3) Many space chamber shrouds have to act as effective traps for simulated solar (or short wavelength) radiation. If the films resulting from the deposit of water vapor have a thickness of less than 0.02 in., the effectiveness of the shroud will not be impaired. For solar wavelengths of greater than 1.1μ, the films will be almost totally absorbing ($\epsilon \geq 0.90$), whereas for solar wavelengths less than 1.1μ, the ice films will be almost totally transparent. Thus for the latter wavelength region, the radiative behavior of the shroud will be the same as before formation of the ice film. A shroud designed to have a high absorptivity for solar radiation will be unaffected by ice deposits of practical thicknesses, since these deposits do not effectively change the local absorptance values of a high-absorptance coating material.
4) Cryodeposits formed on extended surface geometries in the rarified gas regime are nonuniform. Thus the local surface of the extended geometry is not characterized by a single absorptance value and an average value must be used. Consequently, more refined analyses of the effective emittance are not justified.
5) The two-node solution can be used to quickly calculate an emittance value for any particular honeycomb configuration. More generally, the method has utility in the solution of other problems not amenable to exact solutions involving extended surface geometries.

In addition to the preceeding simplified honeycomb analysis, a seven-node analysis was performed. For the seven-node solution, Lockheed's IBM 7090 Thermal Analyzer Program was utilized. To compute the radiation view factors which were required as inputs to the seven-node thermal program, a Lockheed General View Factor Program written for an IBM 7090 was utilized. To accurately compute the necessary configuration factors, the honeycomb cell was broken into forty-two nodes, as is indicated in Fig. 23a. The final analysis consisted of a radiant thermal balance on a seven-node cell. The nodal breakup was as shown in Fig. 23b.

The radiative-computational techniques utilized by the thermal analyzer program are identical to those described in Chapter 4 of Ref. 19. Since the 42-node general view factor program was very complex, only a few cases of general interest were run. Table 2 tabulates for comparison the two- and seven-node effective-emittance results. It indicates that the previously discussed conclusion, that the simplified two-node solution is adequate for the situations of practical interest, is justified.

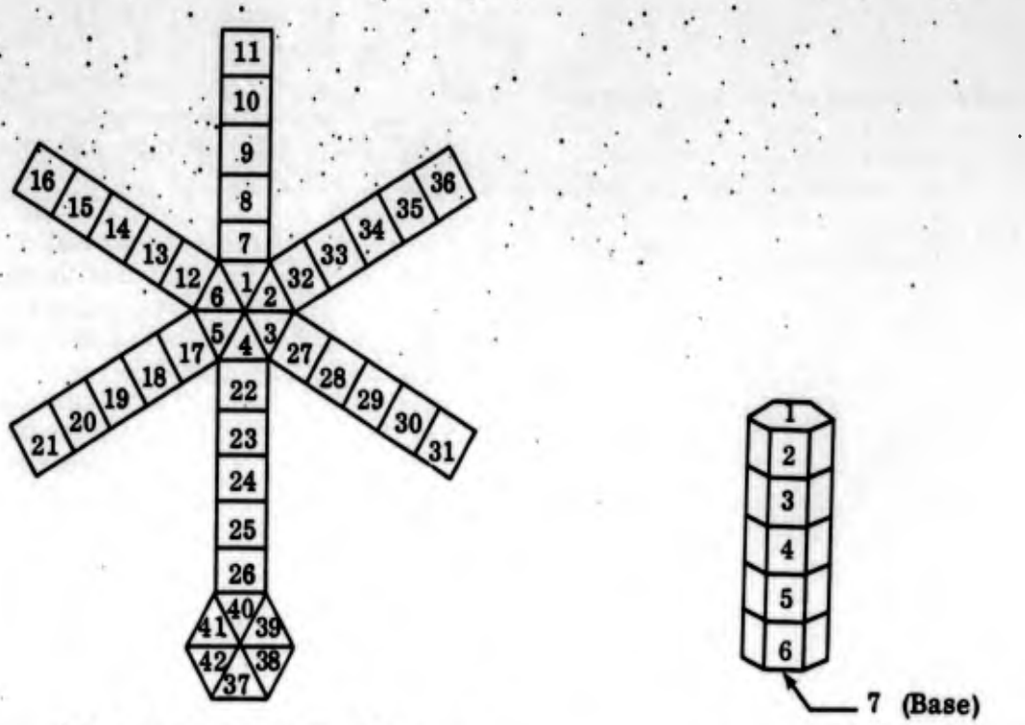

(a) For Use in a Radiant-Energy Configuration Study

(b) For Use in a Radiant Thermal Analysis

Fig. 23 Nodal Break-Up of the Honeycomb Cell

Table 2

EFFECTIVE EMITTANCES OF HONEYCOMB CELLS

M/W	ϵ = 0.5		ϵ = 0.75		ϵ = 0.9	
	7N	2N	7N	2N	7N	2N
1	0.753	0.768	0.878	0.907	0.959	0.968
2	0.821	0.849	0.928	0.944	0.971	0.981

The preceeding analysis for honeycomb assumed that the cell-wall thickness was zero. To compute the effective emittance of a panel of cells, the effective emittance of a composite surface ($\bar{\epsilon}$) consisting of both plain and extended sections must be computed. Thus, $\bar{\epsilon}$ is given by

$$\bar{\epsilon} = \frac{\epsilon A_{edge} + \epsilon_{eff} A_{opening}}{A_{edge} + A_{opening}}$$

For mass-produced honeycomb, the edge area that is common to each cell is given by (see Fig. 24)

$$A_{edge} \simeq 4t\,(W + 0.5774t)$$

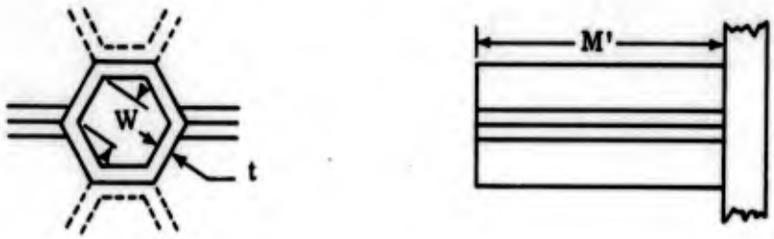

Fig. 24 Mass-Produced Honeycomb Cell Configuration

The plots of $\bar{\epsilon}$ for various configurations of cells are contained in Fig. 22.

Section 5
CONCLUSIONS

(1) The absorptance for 290°K blackbody radiation of opaque films of H_2O or CO_2 at 77°K is high ($\epsilon > 0.9$ for H_2O, $\epsilon > 0.75$ for CO_2), and therefore, the deposition of these gases on the extended cold-wall surfaces facing a test vehicle will not seriously compromise the intended high absorptance of these surfaces.

The H_2O films are opaque to 290°K radiation at a thickness of 0.01 in.; opacity for the CO_2 films does not occur until thicknesses of greater than 0.10 in. However, the effective absorptance of the substrate-condensate system for a condensate film thickness less than the opaque thickness approximates that of the substrate absorptance.

(2) The simulated solar absorptance of an H_2O deposit on a high-absorptance substrate ($\alpha_s = 0.96$) decreases as the coating thickness increases. However, for a coating thickness of less than 0.02 in., the system absorptance is still greater than 0.8. Since this problem is most likely only of practical interest on the extended surface of a chamber cold wall, and since in a practical situation it is unlikely that more than 0.02 in. of deposit could form on an extended surface, it is concluded that the decreasing local absorptance will not present a serious problem.

(3) For thermal radiation characteristic of the cold-wall temperature (80°K to 100°K), the absorptance of the cryopumping surfaces (20°K) is relatively unaffected by deposits of air, N_2, and CO_2. Experiments involving air and N_2 deposits of up to 0.07-in.thickness and CO_2 deposits of 0.09 in. thickness indicate that these films deposited on a low-absorptance substrate do not cause the system absorptance to exceed approximately 0.1. It should be pointed out that it is very unlikely that any significant amounts of cryodeposits could form on the backside of a properly designed cold wall (side facing the cryosurface) and thus it should be relatively easy to reduce the radiant heat transfer between the cold wall and cryo-wall to 1/20 of blackbody to blackbody transfer rates.

This conclusion follows from consideration of the radiant exchange factor between two plane parallel surfaces with emittances of ϵ_1 and ϵ_2. The expression for this factor is

$$\frac{1}{\epsilon_1} + \frac{1}{\epsilon_2} - 1$$

Section 6
REFERENCES

1. A. S. Gilcrest, and G. R. Mon, A Calorimeter for Determining Thermal Radiation Fluxes in Space Simulation Chambers, Institute of Environmental Sciences, 1963 Proceedings
2. P. G. Owston, Advanc. Phys. 7, 171–188 (1958).
3. D. C. Hamilton, W. R. Morgan, Radiant-Interchange Configuration Factors, N. A. C. A., TN 2836, 1952.
4. B. C. Moore, Effect of Gas Condensates on Cryopumps, 1962 American Vacuum Society Meeting, Los Angeles, Calif.
5. L. D. Kislovskii, Optics and Spectroscopy 1, 672 (1956); 2, 186 (1957); 7, 201 (1959)
6. T. M. Cunningham and R. L. Young, Radiative Properties of Cryodeposits at 77°K, ARO Inc., 1962 Cryogenic Engineering Conference, Los Angeles, Calif.
7. J. Dewar, Proc. Phys. Soc. 70, 237 (1902)
8. Mass, Barnes, Proc. Roy. Soc A., III 224, (1926)
9. N. Ockman, Advanc. Phys. 7, 199 (1958)
10. W. E. Osberb and D. F. Hornig, J. Chem, Phys. 20, 1345 (1952)
11. W. Dahlke, Z. Physik 102, 360 (1936)
12. M. M. Fulk and M. M. Reynolds, J. Appl. Phys. 28, 1464 (1957)
13. L. A. Smith, W. E. Keller, and H. L. Johnson, Phys. Rev. 79, 728 (1950)
14. L. A. Smith, W. E. Keller, and H. L. Johnson, J. Chem. Phys. 20, 1572 (1952)
15. E. M. Sparrow, J. L. Gregg, J. V. Szel, and P. Manos, A. S. M. E. Jour of Heat Transfer 83, 207 (1961)
16. L. F. Daws, Brit. Jour. Appl. Phys. 5, 182 (1954)
17. A. K. Oppenheim, A. S. M. E. Trans. 78, 725 (1956)
18. E. M. Sparrow, L. V. Albers, and E. G. R. Eckert, A. S. M. E. Jour. of Heat Transfer, 84, 73 (1962)
19. W. H. McAdams, Heat Transmission 3rd Ed., McGraw-Hill Book Co. (1954)
20. G. R. Smolak, R. H. Knoll, L. E. Wallner, Analysis of Thermal Protection Systems for Space Vehicle Cryogenic Propellant Tanks, Appendix C, NASA TR R-130, 1962
21. S. J. Kline and F. A. McClintock, Describing Uncertainties in Single Sample Experiments, Mech. Eng. 75, 3–8 (1953)
22. M. Jakob, Heat Transfer, John Wiley & Sons, Vol. 2, p. 19 (1956)

Appendix A
DATA ANALYSIS

To determine the absorptance of the cryodeposit on the receiver, it is necessary to determine the net radiant heat transfer rate between the radiator and receiver. Of interest, therefore, is the net energy absorbed by the receiver and the receiver reservoir, for this is the energy that is determined from the measurement of the cryogenic liquid boil-off of the receiver.

A.1 ANALYSIS OF RADIANT ENERGY EXCHANGE

The thermal model for radiant heat transfer between the radiator and receiver is shown in Fig. 25.

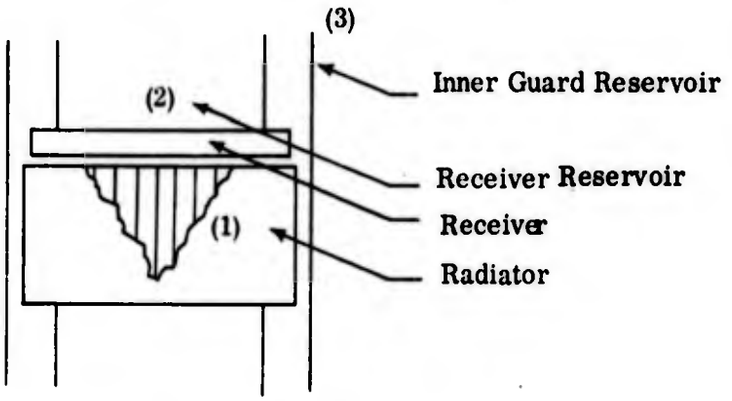

Fig. 25 Calorimeter Thermal Model

The radiant energy-rate interchange terms to be considered are as follows:

(1) q_{12}, the radiant energy emitted by the radiator that is absorbed by the receiver
(2) q_{13}, the sum of the radiant energy that is absorbed on the receiver reservoir (direct radiant interchange with radiator and reflected energy from inner guard walls)
(3) q_2, reemission of energy from the receiver

The net radiant-energy rate absorbed by the receiver and its reservoir is

$$q = q_{12} + q_{13} - q_2 \tag{A.1}$$

It can be shown that the radiant interchange between the radiator and the receiver reservoir and the reflected energy from the inner guard walls to the receiver reservoir (q_{13}) is less than 0.1% of the total energy absorbed by the receiver reservoir for an absorptance as low as 0.05 on the receiver surface. Thus for all practical purposes, the term q_{13} can be neglected from the energy balance of Eq. (A.1).

The net energy rate absorbed by the receiver is then given by the following equation

$$q = q_{12} - q_2 \tag{A.2}$$

The absorbed-energy rate on the receiver that is emitted from the radiator (q_{12}) can be expressed by the equation (Ref. 20)

$$q_{12} = \frac{\sigma\epsilon_1\alpha_2 A_1 F_{12} T_1^4}{1 - F_{12}F_{21}(1 - \alpha_1)(1 - \alpha_2)} \tag{A.3}$$

The conditions that must be fulfilled for Eq. (A.3) to hold are:

- Existence of radiation equilibrium
- Uniform surface temperature on the surface of both the radiator and receiver
- Diffuse emittance of the surfaces
- Grayness of the surfaces

The net emitted energy rate from the receiver can be expressed by the following equation

$$q_2 = \sigma\epsilon_2 A_2 T_2^4 - \frac{\sigma\epsilon_2\alpha_2(1 - \alpha_1)A_2 F_{21} T_2^4}{1 - F_{12}F_{21}(1 - \alpha_1)(1 - \alpha_2)} \tag{A.4}$$

Substituting Eqs. (A.3) and (A.4) into Eq. (A.2) yields an equation for the net radiant energy rate absorbed by the receiver reservoir in terms of the temperature and radiation properties of the radiator and receiver.

$$q = \frac{\sigma\epsilon_1\alpha_2 A_1 F_{12} T_1^4}{1 - F_{12}F_{21}(1 - \alpha_1)(1 - \alpha_2)} - \sigma\epsilon_2 A_2 T_2^4 + \frac{\sigma\epsilon_2\alpha_2(1 - \alpha_1)A_2 F_{21} T_2^4}{1 - F_{12}F_{21}(1 - \alpha_1)(1 - \alpha_2)} \tag{A.5}$$

A.2 ANALYSIS OF CALORIMETER LIQUID BOIL-OFF

The net energy rate absorbed by the receiver is determined by measuring the volume flow rate of gas boil-off of the cryogenic liquid that fills the receiver reservoir.

Two independent methods of measurement were used in series: (1) a wet test gas meter and (2) a predictability flow meter. The wet test gas meter was the most accurate of the two methods for measuring volume flow rate of the gases, and its measurements were used in the data reduction. The predictability meter was used to monitor the gas flow until steady-state conditions were achieved and also served as a check for the readings taken on the wet test gas meter.

To reduce the measured volume flow rate of the wet test gas meters to an energy transfer rate, the following equation was used:

$$q = \dot{v}\left(\frac{d_L}{d_L - d_v}\right)\left(\frac{P_{atm} - P_{W.V.}}{RT}\right) H_v \qquad (A.6)$$

The density ratio $d_L/(d_L - d_v)$ is a correction due to the effective change in volume of the receiver reservoir during vaporization. The term $(P_{atm} - P_{W.V.})$ gives the partial pressure of the calorimeter gas in the wet test gas meter.

A.3 CALCULATION OF RADIANT VIEW FACTORS

The radiant interchange factors are determined from the geometry of the receiver and radiator and the following equation (Ref. 3):

$$F_{12} = \frac{1}{2}\left[x - (x^2 - 4E^2D^2)^{1/2}\right] \qquad (A.7)$$

where

$$x = 1 + (1 + E^2)D^2 \quad ; \quad E = \frac{r_2}{d_{12}} \quad ; \quad D = \frac{d_{12}}{r_1}$$

F_{21} is found by applying the reciprocity theorem. Thus,

$$F_{21} = \frac{A_1}{A_2} F_{12} \qquad (A.8)$$

During the course of the experiment, it was observed that the cryodeposit thickness on the edge of the receiver was approximately one half of the cryodeposit thickness on the face of the receiver. Thus, it was necessary to determine the change in radiant interchange factors as a function of increase in radius of the receiver. The following relation was assumed between the radius of the receiver and the front-face thickness of the cryodeposit:

$$r_2(t') = r_2(0) + \frac{t'}{2} \tag{A.9}$$

A.4 EXPERIMENTAL DATA REDUCTION

A.4.1 Absorptance of 77°K Surface for 290°K Radiation

The solution of Eq. (A.5) for α_2 results in a quadratic equation. One can simplify the solution of α_2 by neglecting the last two terms (reemission from receiver) in Eq. (A.4).

$$q = \frac{\sigma\epsilon_1\alpha_2 A_1 F_{12} T_1^4}{1 - F_{12}F_{21}(1 - \alpha_1)(1 - \alpha_2)} \tag{A.10}$$

Solving for α_2 and assuming $\epsilon_1 = \alpha_1$, one obtains

$$\alpha_2 = \frac{q[1 - F_{12}F_{21}(1 - \alpha_1)]}{\sigma\alpha_1 A_1 F_{12} T_1^4 - qF_{12}F_{21}(1 - \alpha_1)} \tag{A.11}$$

The reemission from the radiator was neglected; thus the maximum error introduced in the absorptance is less than 0.3%.

A.4.2 Solar Absorptance of 77°K Surface

To obtain the solar absorptance of cryodeposits, a Mercury-Xenon lamp was used as a source. The distribution of the source was modified by placing a filter between the lamp

and receiver surface. A honeycomb blackbody receiver was used to calibrate the high-energy source, and a radiation calorimeter was used to monitor the source during tests. The absorptance of the cryodeposit on the receiver surface was obtained by

- Ratioing the energy absorbed by the receiver with the cryodeposit to the energy absorbed by the extended blackbody
- Multiplication by the correction for any change in intensity of the source as detected by the radiation flux calorimeter

A.4.3. Deposit Thickness

The thickness and the density of the deposit was obtained by measuring both the mass of gas metered into the apparatus and the final thickness of the deposit. The mass of gas deposited is given by the following equation:

$$m = CV \frac{\Delta P}{RT} \tag{A.12}$$

where C is a constant and is the ratio of the total gas injected to that deposited on the receiver. (The value of C is determined by the ratio of the area of the receiver to the inside area of the teflon ring.) The density and the intermediate thickness is given by the following equations:

$$d = \frac{m}{At'} \tag{A.13}$$

and

$$t' = \frac{\Delta P}{\Delta P_F} t'_F \tag{A.14}$$

where subscript F refers to final values

Appendix B
ERROR ANALYSIS

The error in the absorptance of a 77°K surface for 290°K radiation is calculated by means of the method outlined in Ref. 21. This method was designed to estimate the propagation of experimental uncertainties into the results of single-sample experiments and is well suited to the prediction of the maximum possible experimental error in the measurements of absorptance

The simplified equation (A. 11) for absorptance discussed in Appendix A is the most convenient for describing the maximum possible probable error in the absorptance:

$$\alpha_2 = \frac{q[1 - F_{12}F_{21}(1 - \alpha_1)]}{\sigma\alpha_1 A_1 F_{12} T_1^4 - qF_{12}F_{21}(1 - \alpha_1)} \tag{B.1}$$

The maximum experimental error in the absorptance can be represented in terms of the controlling variables of Eq. (B. 1)

$$\delta\alpha_2 = \frac{\Delta\alpha_2}{\alpha_2} = \frac{\partial\alpha_2}{\partial q}\frac{\Delta q}{\alpha_2} + \frac{\partial\alpha_2}{\partial F_{12}}\frac{\Delta F_{12}}{\alpha_2} + \frac{\partial\alpha_2}{\partial F_{21}}\frac{\Delta F_{21}}{\alpha_2} + \frac{\partial\alpha_2}{\partial\alpha_1}\frac{\Delta\alpha_1}{\alpha_2} + \frac{\partial\alpha_2}{\partial A_1}\frac{\Delta A_1}{\alpha_2} + \frac{\partial\alpha_2}{\partial T_1}\frac{\Delta T_1}{\alpha_2} \tag{B.2}$$

With use of the experimental results of the deposit of CO_2 on a plain aluminum substrate, the maximum possible experimental error in the absorptance was 8% for a low absorptance ($\alpha_2 = 0.06$) and 6% for a high absorptance ($\alpha_2 = 0.72$). These results for maximum error in aborptance are typical for all the other CO_2 deposits and the H_2O deposits. Although the maximum experimental errors based on the analysis technique of single-sample observations are quite high, the chances that the terms in Eq. (B. 2) are additive, that is all in the direction to give the maximum error, are improbable. Because excellent reproducibility of experimental results was obtained when tests were repeated, the experimental error in absorptance is conservatively estimated to be less than 5%. By using the same analysis as outlined above, the measurement of solar absorptance is estimated to have an experimental error of 5%.

The error in thickness and/or density of the deposit can be calculated in a manner similar to the calculation of error in absorptance. However, the error in the measurement of the thickness is much greater than any of the other experimental errors. The experimental uncertainties actually observed in determining the densitites of the 77°K cryodeposits were 11% for H_2O and 12% for CO_2.

Appendix C

MATHEMATICAL ANALYSIS OF THE EMITTANCE OF A LONG V-SHAPED GROOVE

The relevant parameters for the analysis of the emittance of a V-shaped groove are shown in Fig. 26. The total radiant flux leaving a position x on one leg of the V-groove (Ref. 15) is

$$B(x) = \epsilon\sigma T^4 + \rho H(x) \tag{C.1}$$

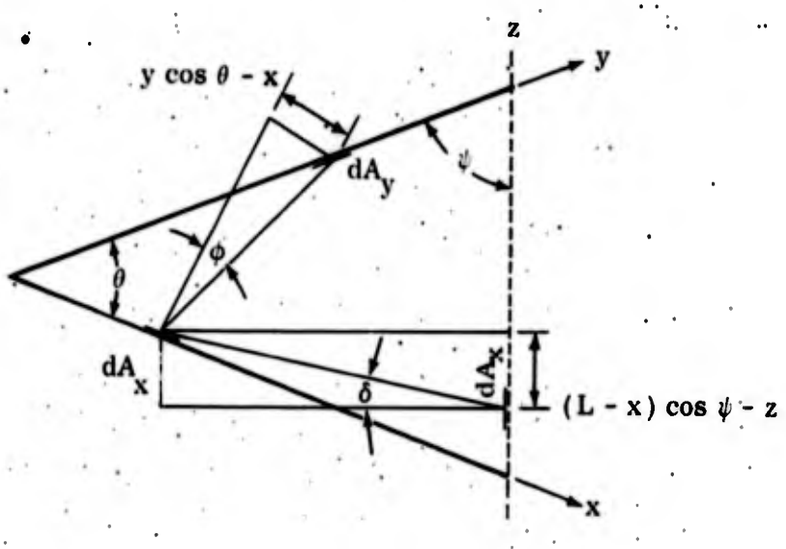

Fig. 26 V-Groove Nomenclature

The term H(x) must be determined. Consider the fact that the total energy leaving an elementary area on y is $B(y)\,dA_y$. Of this amount, $B(y)\,dA_y\,dF_{y-x}$ arrives at an element of area dA_x on surface x. But, by reciprocity $dA_y\,dF_{y-x} = dA_x\,dF_{x-y}$. Therefore $B(y)\,dA_x\,dF_{x-y}$ impinges on the element of area dA_x. The energy impinging on unit area at x due to radiation leaving dA_y is thus $B(y)\,dF_{x-y}$. The area dA_x receives energy from all positions on y. The total energy H(x) received by unit area at position x is

$$H(x) = \int_{y=0}^{L} B(y)\,dF_{x-y} \tag{C.2}$$

From Jakob, Ref. 22, we have

$$dF_{x-y} = \frac{1}{2} d(\sin \phi) \tag{C.3}$$

By reference to Fig. 26 we have

$$\sin \phi = \frac{y \cos \theta - x}{\sqrt{(y \cos \theta - x)^2 + (y \sin \theta)^2}} \tag{C.4}$$

With the result that

$$d(\sin \phi) = \frac{xy(1 - \cos^2 \theta)\, dy}{(x^2 + y^2 - 2xy \cos \theta)^{3/2}} \tag{C.5}$$

Substitution of Eqs. (C.2, C.3, and C.5) into Eq. (C.1) results in

$$B(x) = \epsilon \sigma T^4 + \frac{\rho}{2} \int_{y=0}^{L} B(y) \frac{xy(1 - \cos^2 \theta)\, dy}{(x^2 + y^2 - 2xy \cos \theta)^{3/2}} \tag{C.6}$$

which in dimensionless form becomes

$$\beta(X) = 1 + \rho \frac{(1 - \cos^2 \theta)}{2} \int_{Y=0}^{1} \beta(Y) \frac{XY\, dY}{(X^2 + Y^2 - 2XY \cos \theta)^{3/2}} \tag{C.7}$$

where

$$\beta(X) = \frac{B(x)}{\epsilon \sigma T^4}, \quad \beta(Y) = \frac{B(y)}{\epsilon \sigma T^4}, \quad X = x/L, \quad Y = y/L$$

Because of symmetry, $\beta(X) = \beta(Y)$ obtains. Thus solution of Eq. (C.7) provides the radiosity $\beta(X)$ or $\beta(Y)$.

It is now possible to determine $H(z)$, the flux leaving the groove. The total energy leaving an element area dA_x on surface x is $B(x)dA_x$. Of this amount, $B(x)dA_x : dF_{x-2}$ arrives at an element of area on surface z. But $dA_x dF_{x-z} = dA_z dF_{z-x}$. Therefore $B(x)dA_z dF_{z-x}$ impinges on the element of area dA_z. The energy impinging on unit area at z due to radiation leaving dA_x is thus $B(x)dF_{z-x}$. The area dA_z receives energy from all positions on x. The total energy flux received at position z due to energy leaving surface x is

$$H(z)_x = \int_{x=L}^{0} B(x)\, dF_{z-x} \tag{C.8}$$

From Jakob, Ref. 22, we have

$$dF_{z-x} = \frac{1}{2}\, d(\sin \delta) \tag{C.9}$$

By reference to Fig. 26 we obtain

$$\sin \delta = \frac{(L - x)\cos \psi - z}{\sqrt{\left[(L - x)\cos \psi - z\right]^2 + \left[(L - x)\sin \psi\right]^2}}$$

with the result that

$$d(\sin \delta) = \frac{z(x - L)(1 - \cos^2 \psi)\, dx}{\left[z^2 + (L - x)^2 - 2z(L - x)\cos \psi\right]^{3/2}} \tag{C.10}$$

Eq. (C.8) thus becomes

$$H(z)_x = \frac{1}{2}\int_{x=L}^{0} B(x)\frac{z(x-L)(1-\cos^2\psi)\,dx}{\left[z^2+(L-x)^2-2z(L-x)\cos\psi\right]^{3/2}} \qquad (C.11)$$

Because of the symmetry of the V-groove, the incident flux from side y is

$$H(z)_y = H(M-z) = \frac{1}{2}\int_{x=L}^{0} \frac{B(x)(M-z)(x-L)(1-\cos^2\psi)\,dx}{\left[(M-z)^2+(L-x)^2-2(M-z)(L-x)\cos\psi\right]^{3/2}} \qquad (C.12)$$

Therefore, the total flux leaving the groove opening at a position z is

$$H(z) = \frac{1}{2}\int_{x=L}^{0} B(x)\frac{z(x-L)(1-\cos^2\psi)\,dx}{\left[z^2+(L-x)^2-2z(L-x)\cos\psi\right]^{3/2}}$$

$$+\frac{1}{2}\int_{x=L}^{0} B(x)\frac{(M-z)(x-L)(1-\cos^2\psi)\,dx}{\left[(M-z)^2+(L-x)^2-2(M-z)(L-x)\cos\psi\right]^{3/2}} \qquad (C.13)$$

In dimensionless form, Eq. (C.13) becomes:

$$\bar{H}(Z) = \frac{1}{2}\int_{X=1}^{0} \frac{\beta(X)\left[Z(X-1)(1-\cos^2\psi)\right]\,dX}{\left[Z^2+(1-X)^2-2Z(1-X)\cos\psi\right]^{3/2}}$$

$$+\frac{1}{2}\int_{X=1}^{0} \frac{\beta(X)(\bar{M}-Z)(X-1)(1-\cos^2\psi)\,dX}{\left[(\bar{M}-Z)^2+(1-X)^2-2(\bar{M}-Z)(1-X)\cos\psi\right]^{3/2}} \qquad (C.14)$$

The total energy (H_T) leaving the groove is

$$H_T = \int_{z=0}^{M} H(z)\, dz \tag{C.15}$$

which, in dimensionless form, becomes

$$\bar{H}_T = \int_{Z=0}^{\bar{M}} \bar{H}(Z)\, dZ \tag{C.16}$$

The emittance of the V-groove is

$$\epsilon_{eff} = \frac{H_T}{M\sigma T^4} = \frac{1}{M\sigma T^4} \int_{z=0}^{M} H(z)\, dz \tag{C.17}$$

which can be written

$$\epsilon_{eff} = \frac{\epsilon}{\bar{M}} \int_{Z=0}^{\bar{M}} \bar{H}(Z)\, dZ \tag{C.18}$$

UNCLASSIFIED